Energy Compensation of Multi-bunch Beam for Linear Colliders

Shigeru KASHIWAGI

Doctor of Science

Department of Accelerator Science,
School of Mathematical and Physical Science,
The Graduate University for Advanced Studies

March, 1999

Contents

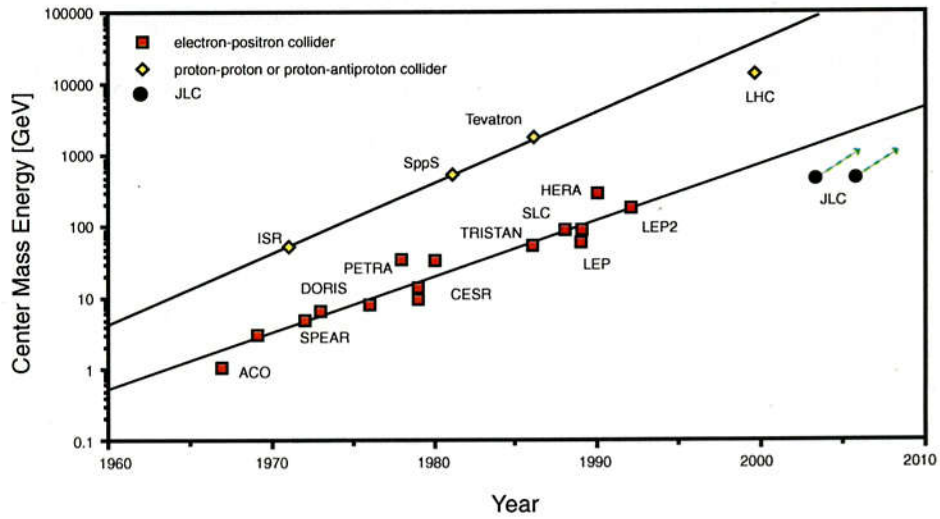

Figure 1.1: The energy frontier of particle physics.

1 Introduction

1.1 Background

1.1.1 Linear colliders

High energy accelerator have been used to study the fundamental properties of matter at high energies. In such colliders, beams of charged particles in opposite directions collide at one or several interaction points. The colliding beams can be either hadron-hadron, electron-positron, or hadron-electron. In these different types of particle collisions, the physical understanding from the interactions produced is different, therefore all three kind of colliding beams are needed. As results using hadron collider, the $W^{\pm}$ and Z_0 bosons have been observed at CERN (European Center for Nuclear Research), the top quark has discovered at the Tevatron in FNAL (Fermi National Accelerator Laboratory). Electron-positron colliders provide clear experimental environments in which precise measurements can be made. As major results by experiments at electron-positron colliders, the discoveries of charm quark and τ lepton at SPEAR , discovery of the gluon and establishment of QCD at PETRA and PEP, and precision exploration of electroweak phenomena at the SLC and LEP (Large Electron-Positron) [1].

For the future energy frontier physics, the center-mass energy is desired to be as high as 1 TeV. Protons have a large mass compared to electrons mass, therefore it is possible to achieve the higher energy without synchrotron

radiation loss. In Europe there is the Large Hadron Collider (LHC) project which aim at an energy above 10 TeV.. The electron-positron collider also is desired for both discovery and precision measurement. To advance our understanding of particle physics at the TeV scale, both hadron-hadron and electron-positron colliders will be required.

At high energies the radiation loss is larger for circular acceleration than for linear acceleration. In addition, the radiation loss is much worse for accelerating light electrons than for heavier protons. Electrons and positrons can be brought to high energies only in linear accelerators or in circular ones with large radius. The circulating electrons or positrons continually lose energy by synchrotron radiation in a circular collider. The energy loss per turn (ΔE) due to synchrotron radiation varies as the fourth power of the beam energy (E), and inversely as the machine radius (ρ) (Eq. 1.1)

$$\Delta E = \frac{4\pi e^2}{3(m_0 c^2)^4} \cdot \frac{E^4}{\rho} \tag{1.1}$$

where e, m_0 and c are electron charge magnitude, electron rest mass and speed of light respectively. This energy loss has to be made up by RF accelerating cavities in turn. The largest electron-positron collider in operation is the LEP collider and it has a circumference of 27 km and is currently being operated at an energy of about 75 GeV per beam. It is upgraded to an energy about 100 GeV per beam (LEP-II) [1]. In the case of the LEP-II, the energy loss per turn is about 2.84 GeV per electron at 100 GeV. It is generally agree that the next electron-positron collider is to be at least 500 GeV center of mass, and at this energy the circular electron-positron collider would be as large as several hundred kilometers of a circumference. To overcome this radiation limit of the circular colliders, the only possible electron-positron accelerator for TeV energy range is the linear collider.

The world's first linear collider is the SLAC linear accelerator (SLC) which has already been built and operated at Stanford Linear Accelerator Center (SLAC). The operation of SLC has proved the possibility of future electron-positron linear colliders as the powerful tool of the particle physics experiment over 100 GeV center mass energy.

The new electron-positron linear colliders are planned to be at energy range 0.5-1.5 TeV center of mass in the world, CLIC [2], SBLC [3][4], TESLA [5], NLC [6], VLEPP [7], JLC [8], and the R&D for there projects has been performed to realized the electron-positron linear colliders.

There are mainly two difficult techniques for future linear collider. One is the high gradient acceleration to achieve the high energy within short length, another one is extremely small beam size to get high luminosity at collision point. The former technique is depends on the total rf system and the accelerating structure, the research and study for this technique are

carried out at the laboratories in the world. For latter technique, the FFTB (Final Focus Test Beam) [9] [10] experiment to make a extremely small size beam was performed at SLAC by international collaboration. As the result, beam was focused to 67 nm in vertical beam size and measured the beam spot size by the Shintake beam size monitor [11] [12] and LAY-ORSAY gas monitor [13][14]. The success of FFTB experiment is significant advance for the future linear colliders. As another development, there is the generation of the extremely low emittance beam at ATF (Accelerator Test Facility) in KEK. Since finally focussed beam size is depend on the beam emittance, the future linear colliders need the the extremely low emittance beam.

Further there are some issues to be studied, the multi-bunch acceleration to get the high luminosity, the wakefield which includes the multi-bunch effect such as the beam loading and multi-bunch instability, an alignment of accelerator components, the beam instrumentation and so on.

In this paper, we described the study for the multi-bunch energy compensation including the tracking simulation and the beam test in ATF linac.

1.1.2 Multi-bunch Beam

The experiment of particle physics require a large number of events per seconds produced in particle interaction. The event rate of physical process (Y) equal to the product of the cross section (σ) and the luminosity (L).

$$Y = L\sigma \tag{1.2}$$

The cross section of weak interaction is in inverse proportion to square of the center-mass energy. Therefor the luminosity of the linear collider have to increase in proportion to square of the center-mass energy. In the case of that the center mass energy of the linear collider is 0.5 TeV, the luminosity is at least required $3\times10^{33}\ cm^{-2}sec^{-1}$. Luminosity (Geometric luminosity) is given by

$$L = \frac{N^2 n_b f_r}{4\pi\sigma_x^*\sigma_y^*}. \tag{1.3}$$

Here $N_+, N_-, n_b, f_r, \sigma_x^* and \sigma_y^*$ are the number of electrons and positrons per bunch , the number of bunches accelerated per rf pulse, the rf repetition rate in linac, the root mean square (rms) bunch width and height (Gaussian bunches are assumed), respectively. In this equation the change of bunch shape and complicated effect during the collision process don't take into account [15]. The total energy of electron and positron beam (P_b) is related to the wall-plug power.

$$P_b = n_b \eta_{rf} \eta_s \eta_b P_{wall} = n_b \eta P_{wall} \tag{1.4}$$

Here η_{rf} is the conversion efficiency from ac power to rf power, η_s is a stored efficiency of rf power in the accelerating structure which takes into account the power loss at the walls of waveguide, pulse compression system and structure, η_b is an accelerated efficiency per bunch in the structure, η is conversion efficiency from ac power into beam power [16][17].

As another expression, total beam energy at interaction point can be expressed by

$$P_b = n_b(N_+ + N_-)E_b f_r = 2n_b N E_c f_r, \tag{1.5}$$

where number of electron and positron are same and E_b, E_c are each beam energy and center-mass energy , respectively. (E_c=$2E_b$ is assumed).

From Eq. 1.3, 1.5 and 1.4, the luminosity is expressed as

$$L = \frac{N}{4\pi\sigma_x^*\sigma_y^*}\frac{n_b \eta P_{wall}}{E_c}. \tag{1.6}$$

In case that η, P_{wall} and E_c are fixed, the luminosity is in proportion to the bunch population (N) and the number of particle per bunch (n_b) and is in inverse proportion to the beam size. The bunch population is mainly limited by the beamstrahlung [18] and the positron generation. For instance in the linac of the KEK JLC design [8], the bunch population is $0.7\sim$ $1.2 \times 10_{10}$ particle/bunch. The minimum beam size depends on the beam emittance [19]. Therefor the multi-bunch acceleration ($n_b \geq 1$) is necessary to get high luminosity in the linear collider.

1.1.3 Japan Linear Collider

The target of future linear collider is the center mass energy range of 0.5 to 1.5 TeV and luminosity around 1×10^{34} /cm^2/sec. These future linear colliders are planned and designed, and some design reports for future linear colliders were already published from the accelerator laboratories in the world. In Japan, the study for future linear collider has been performed under the collaboration with many universities, companies and laboratories. In KEK the normal conducting linear colliders are planned, the accelerating frequency choice of future linear colliders has been discussed from many years ago as important issue. In this paper, we mainly discuss using KEK-JLC design. The future linear colliders will be consisted of the following parts:

1. Electron and positron source

— Fundamental Parameters —			
Main accelerating frequency	f_{rf}	11.424	GHz
Number of particles per bunch	N	0.70×10^{10}	
Number of bunches per pulse	m_b	85	
Bunch spacing	t_b	1.40	nsec
Repetition frequency	f_{rep}	150	Hz
Normalized emittance at damping ring exit	$\gamma\varepsilon_x/\gamma\varepsilon_y$	$3 \times 10^{-6}/3 \times 10^{-8}$	m·rad
R.m.s. bunch length	σ_z	90	μm

Table 1.1: A fundamental beam parameters for the X-band JLC which are independent of the beam energy.

2. Injector linacs
3. Damping ring
4. Bunch compressor
5. Main linacs
6. Final focus and Interaction point

, Figure 1.2 shows a schematic layout of diagram of JLC. Table 1.1 gives a fundamental beam parameters for the KEK-JLC X-band linear collider.

As shown in Table 1.1, the multi-bunch beam of small bunch spacing are generated and accelerated in the linacs. The multi-bunch acceleration introduces the multi-bunch effect due to the transverse and longitudinal wakefield.

1.2 Multi-bunch acceleration

1.2.1 Longitudinal motion

The charged particle is accelerated by the electric field in an accelerating structure of traveling wave. Throughout this paper, we assumed that the group velocity of structure is very slow in comparison with the speed of light. Thus, during a bunch pass through the structure, there is no propagation of wake field. In the following, we will discuss about the constant gradient (C.G.) accelerating structure and we assumed that the shunt impedance and Q-value of structure are constant over the length of an accelerating structure approximately [20].

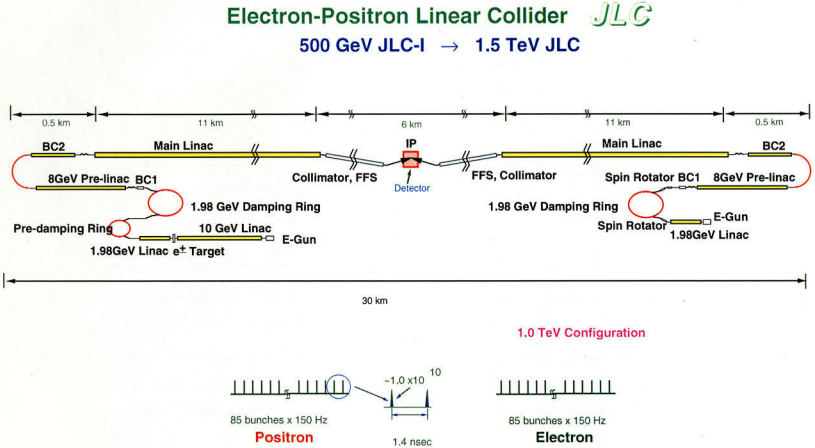

Figure 1.2: The layout of the Japan Linear Collider

The energy gain of a charged particle in an accelerating structure of length L is

$$\Delta E_{acc} = e \int_0^L E(s) ds. \tag{1.7}$$

Here the $E(s)$ is the accelerating field as a function of distance along the structure. From Eq. 1.7 we need to know the distribution of accelerating field along the structure for the calculation of energy gain.

Rf power propagates at group velocity v_g and gradually attenuate due to resistive wall loss in the accelerating structure. Rf power attenuation is like

$$P(s) = P_0 e^{-\int_0^s 2\alpha ds} = P_0 e^{-\int_0^s \frac{\omega}{v_g(s)Q} ds} \tag{1.8}$$

where P_0, ω, Q and α are input rf power level, rf frequency, Q-value of structure and attenuation parameter per unit length, respectively. The attenuation parameter relates with the attenuation constant as following equation.

$$\tau = \int_0^L \alpha(s) ds = \int_0^L \frac{\omega}{2 v_g(s) Q} ds \tag{1.9}$$

The accelerating field at s along the structure as function of time is given by

$$\begin{aligned} E(s,t) &= \sqrt{r_0 (-\frac{-dP(s,t)}{ds})} = \sqrt{2\alpha r_0 P(s,t)} \\ &= \sqrt{\frac{\omega r_0}{v_g(s) Q} P(s, t-t') e^{-\int_0^s \frac{\omega}{2 v_g(s) Q} ds}} \end{aligned} \tag{1.10}$$

where r_0 is shunt impedance per unit length and t' is input power level at time (t-t'), respectively. Here t' is

$$t' = \int_0^s ds' \frac{1}{v_g(s')} \tag{1.11}$$

Therefore, the energy gain of charged particle in an accelerating structure is

$$\Delta E_{acc} = e \int_0^L \sqrt{\frac{\omega r_0}{v_g(s) Q} P_{s,t-t'}} e^{-\int_0^s \frac{\omega}{2 v_g(s) Q} ds} ds. \tag{1.12}$$

Next we consider the longitudinal wake field which is induced in the fundamental accelerating mode by short bunch.

When short bunch is injected into the structure with speed of light, the fundamental longitudinal wake field is excited in the structure and it is expressed as

$$E_{wake} = -\frac{r_0 \omega}{2Q} q = -2kq \tag{1.13}$$

where k is the loss factor per unit length of fundamental mode and this parameter is defined as $k \equiv r\omega/4Q$ [21][22][23]. In case that bunch length is sufficiently shorter than the wavelength of the fundamental mode, the longitudinal wake field is approximately constant within bunch length. Then the average energy loss of the short bunch due to wake field in a structure is given by

$$\Delta E_{short-bunch} = -ekqL. \tag{1.14}$$

After the bunch traverses the structure, the excited field propagates in the structure at the group velocity. In case that the wake field propagate from s_0 to s_1 within time t, the propagating fields at s_1 is expressed as

$$t = -\int_{s_0}^{s_1} \frac{ds}{v_g(s)} \tag{1.15}$$

$$E_{wake}(s_1) = -2kq\sqrt{\frac{(r_0\omega/v_g(s_1)Q)_{s_1}}{(r_0\omega/v_g(s_0)Q)_{s_0}}}e^{-\int_{s_0}^{s_1}\frac{\omega}{2v_g(s)Q}ds}. \tag{1.16}$$

Suppose that the second bunch is injected into the structure at time t after the first bunch injection, the voltage felt by second bunch (ΔV_{bl}) due to the excited field of proceeding bunch in the structure is

$$\Delta V_{bl}(t) = -\int_{s_{00}}^{L} ds_1 E_{wake}(s_1) \tag{1.17}$$

where s_{00} is the propagation distance of wake field from first particle injection to second one injection. In the case of the constant gradient accelerating structure, s_{00} and ΔV_{bl} are given by

$$s_{00} = \frac{L(1-e^{-2\tau t/t_f})}{1-e^{-2\tau}} \quad (t \le t_f) \tag{1.18}$$

$$= L \quad (t \ge t_f) \tag{1.19}$$

$$\Delta V_{bl} = -2kq(L - s_{00}(t)) \tag{1.20}$$

$$= -2kqL\left[1 - \frac{1-e^{-2\tau t/t_f}}{1-e^{-2\tau}}\right] (t \le t_f) \tag{1.21}$$

$$= 0 \quad (t \ge t_f) \tag{1.22}$$

This voltage is the sum of the excited longitudinal wake field by one leading bunch.

Next we apply the Eq. 1.20 to the multi-bunch beam which has n_{bl} bunches with charge eN. In this case the bunch population of all bunches

in a train is same and bunch spacing is constant with t_{sp}. Because of the bunch spacing is much smaller than the filling time of accelerating structure, in following the multi-bunch beam will be considered as continuous current i_0 which is expressed as

$$i_0 = eN/t_{sp} \tag{1.23}$$

The loading voltage of nth bunch (V_{bl}) injected at $t_{inj} = (n-1)t_{sp}$ after the first bunch injection is derived from following equation.

$$V_{bl,n} = \frac{r_0 i_0 L}{2}\left[\frac{2\tau e^{-2\tau}}{(1-e^{-2\tau})}\frac{t}{t_f} - \frac{1-e^{-2\tau t/t_f}}{1-e^{-2\tau}}\right] \quad (t_{inj} \le t_f) \tag{1.24}$$

$$= \frac{r_0 i_0 L}{2}\left[\frac{2\tau e^{-2\tau}}{(1-e^{-2\tau})} - 1\right] \quad (t_{inj} \ge t_f) \tag{1.25}$$

Therefore, the total accelerating voltage of nth bunch is

$$\Delta V_{total} = \int_0^L E(s)ds - eNkL + \Delta V_{bl,nth}. \tag{1.26}$$

For instance in the linac of the KEK JLC design [8], a bunch train consists of 85 bunches of 7.2×10^9 electrons/bunch with 1.4 ns bunch spacing. The instantaneous beam current of the JLC linac is evaluated to be 0.823 A at N_{bl}=7.2×10^9 electrons per bunch. The energy loss of the last bunch in a 3 m-long structure is evaluated to be 10.6 MeV. The energy distribution of the bunches accelerated in a 3 m-long accelerating structure is shown in Figure. 1.3. In this calculation, the s-band accelerating structure has the parameters in Table 1.2.

In the s-band linac, as the pulse length of a multi-bunch beam is shorter than the filling time of accelerating structures, the energy gain of successive bunches drops by approximately linear function due to a transient beam loading in the accelerating structures. This energy spread is critical for lattice design. Not properly compensated,it will induce emittance growth and in turn lower the luminosity of the machine. So in future linear colliders, it is necessary to compensate the beam loading by some energy compensation technique.

1.2.2 Transverse motion

We consider the motion of a particle in any linear focusing lattice. The particle oscillate around the center trajectory which is ideal orbit in a linac. The equation of transverse motion is given by

$$\frac{1}{\gamma(s)}\frac{d}{ds}\left[\gamma(s)\frac{d}{ds}x(s)\right] = -\frac{1}{\beta(s)^2}x(s) \tag{1.27}$$

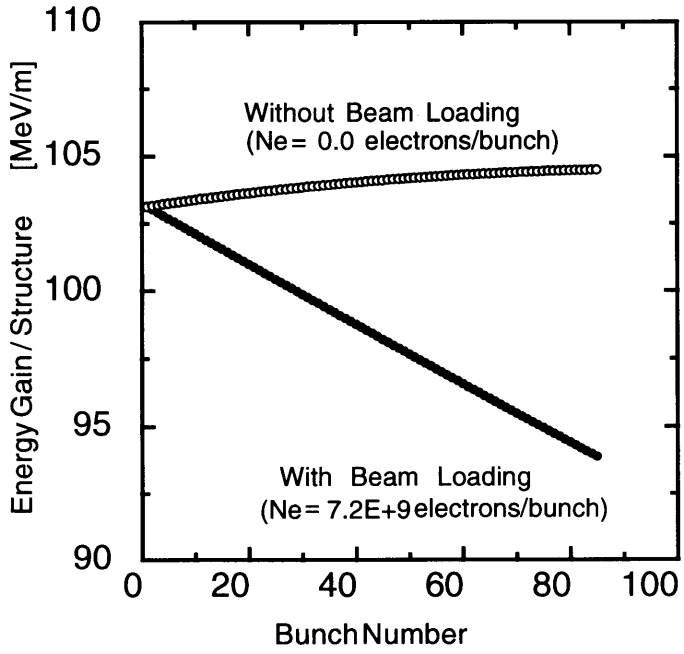

Figure 1.3: Energy gain of multi-bunches in a 3 m-long accelerating structure with and without beam loading

Table 1.2: Main parameter of s-band accelerating structure

Operation frequency	2856 MHz
Phase shit / cell	$2\pi/3$
Electric-field distribution	Constant gradient
Structure length	3 m
Number of cell	84 cells + 2 couplers
Quality factor	13,000
Shunt impedance	60 MΩ
Attenuation parameter	0.57
Group velocity	0.0204 - 0.0065 c
Filling time	830 ns

where $x(s)$, $\gamma(s)$ and $\beta(s)$ is the transverse displacement of a particle, the Lorentz factor and the beta-function at position s along the linac, respectively. Since we assume that the changing of $\gamma(s)$ and $\beta(s)$ is smooth, $\gamma(s)''$ and $\beta(s)''$ are equal to zero [24][25][26]. The displacement of particle can be solved from Eq. 1.27 approximately

$$x(s) = x(0)\sqrt{\frac{\beta(s)\gamma(0)}{\beta(0)\gamma(s)}}\cos\psi(s) \tag{1.28}$$

where $\psi(s)$ is phase advance

$$\psi(s) = \int_0^s \frac{1}{\beta} ds \tag{1.29}$$

As initial condition, we assumed the following relation

$$\left.\frac{dx(s)}{ds}\right|_{s=0} = 0 \tag{1.30}$$

We next consider the two particle in the linac which are a leading particle and following particle. The distance of two particles is z and the transverse displacement of the leading and following at location s are $x_1(s)$ and $x_2(s)$, respectively. The charge of leading and following particle are q and e. Since the dipole-mode wake field felt by following particle is proportional to the offset of leading particle, wake field force has a time dependence of betatron oscillation frequency. Suppose that the dipole-mode wakefunction at s is $W_T(z)$ which is constant along the linac, the following particle feel the transverse force which is expressed as

$$F_T(s) = eqx_1(s)W_T(z) \tag{1.31}$$

The equation of transverse motion for the following particle is given by

$$\frac{1}{\gamma(s)}\frac{d}{ds}\left[\gamma(s)\frac{d}{ds}x_2(s)\right] = -\frac{1}{\beta(s)^2}x_2(s) + \frac{1}{m_0c^2\gamma(s)}F_T(s). \tag{1.32}$$

The displacement of following bunch is

$$x_2(s) = x_2(0)\sqrt{\frac{\beta(s)\gamma(0)}{\beta(0)\gamma(s)}}\left\{\cos\psi(s) + \frac{eqW_T(z)}{2m_0c^2}\left(\int_0^s \frac{\beta(s)}{\gamma(s)}ds\right)\sin\psi(s)\right\} \tag{1.33}$$

The second term of Eq. 1.33 is the oscillation due to wake field effect. The amplitude of oscillation increases along the linac.

In the single bunch, we can roughly estimate by replacing the distance of two particle z and the charge q with the bunch length σ_z and bunch

charge, respectively. We will discuss the method of suppressing or reducing the this increasing oscillation in following section. However, the single bunch instability due to the short range wake field is connected to the iris size of the accelerating structure. Higher frequency band linac, alignment tolerance of the accelerating structures and straightness tolerance for a structure will be tighter.

In the multi-bunch operation, the deflected beam by wake field of leading bunch will excite a deflection mode in the structure, which will deflect more the following bunch in a train. There is a coupling in the motion of bunches. In case that the initial beam offset and optics parameters (beta functions, phase advance and so on) are same, we have to reduce the dipole-mode wakefunction to be small coupling. Recently a variety of structures are developed to control or damp the long-range transverse wake field for the future linear colliders, the detuned structure [27], the damped detuned structure [28], the choke mode (Shintake type choke mode) structure [29], for example. Multi-bunch instability can be control or does not occur using there structure.

In the following section, we will replace the smooth focusing approximation by the more realistic alternating-gradient focusing which is like a FODO lattice, and will carry out the tracking simulation [30].

1.3 Purpose of this research and significant

For future linear colliders, one of essential technique to get sufficient luminosity is the ability to accelerate the multi-bunch beam with small bunch spacing. In multi-bunch acceleration, it is important to control the transverse and longitudinal wakefields. The transverse wakefields in the accelerating structures cause the multi-bunch instability and the longitudinal wakefields induce the energy deviation due to the beam loading in the structures. If the energy deviation is not compensated, the emittance growth is introduce and in turn lower the luminosity. So the compensation of the bunch-to-bunch energy spread is essentially important for future linear colliders.

In this paper, we compare with the two different types of multi-bunch energy compensation method for the emittance growth in the linacs using tracking simulation, one is local compensation method and another one is unlocal energy compensation method. The results of this simulation will be good information for design of future linear colliders.

We describe the beam tests for the energy compensation methods using the multi-bunch beam at the ATF linac in KEK.

The purpose of this research is to consider the multi-bunch energy compensation method from the both side the simulation and experiment.

2 Energy compensation method of multi-bunch beam

2.1 Rf pulse compression system and beam loading

In future linear collider, a beam has to achieve high energy within limited length, therefore the high accelerating gradient is required. High accelerating gradient needs high peak power. To obtain high peak power, a linac rf system needs the rf pulse compression systems. The rf pulse compression system is desirable for reducing the number of klystrons and klystron modulators to save the total cost of a linac. The rf pulse compression system will influence the total rf system of linacs. For multi-bunch operation in linear colliders the choice of the energy compensation method connects with the rf pulse compression system.

Until now, BPM (Binary Power Multiplier) [31], SLED-II [32] and DLDS (Delay Line Distribution System) [33] were developed or devised to get a rectangular rf pulse. The BPM system multiplies the rf power by 2^n using 3 dB hybrid combiner and delay line. The SLED-II stores rf power in resonant delay line, and to get a compressed flat pulse the input rf phase is reversed. This SLED-II rf pulse compression system has developed as rf system for the X-band next linear collider (NLC) at SLAC. In DLDS rf power is distributed to accelerating structure using delay line of low-loss waveguides. The time of beam traverse from upstream accelerating structure is canceled by the time of rf propagation to structure in delay lines. Now rf components for DLDS are developing at KEK, SLAC and BINP. However these rf pulse compression systems need long delay line whose length is determined by the filling time of accelerating structure. It is difficult to applicate these compression system in lower frequency linac, since the length of delay line will be very long.

Recently a pulse compression system using the multi-cell coupled cavity system [34] [35] was developed by C-band linear collider group in KEK. By amplitude modulation on the input rf power to compressor, this compression system obtain the flat output pulse from the rf pulse compressor. In the amplitude modulation, two klystrons are used and rf phases of two klystrons are rotated into opposite direction to each other and rf power are combined using 3-dB hybrid combiner. As the result, the phase modulation is converted to the amplitude modulation, and the phase of input rf to compressor is kept at constant [34]. The advantage of this compression system is that the flat pulse is generated with high gain and good efficiency, the arbitrary waveform also can be generated by controlled amplitude of the input rf pulse. This means that this compression system can be applied to non-uniform multi-bunch beam. This compression system was considered synthetically including multi-bunch energy compensation.

In the S-band linac, the pulse compression system based on the SLED

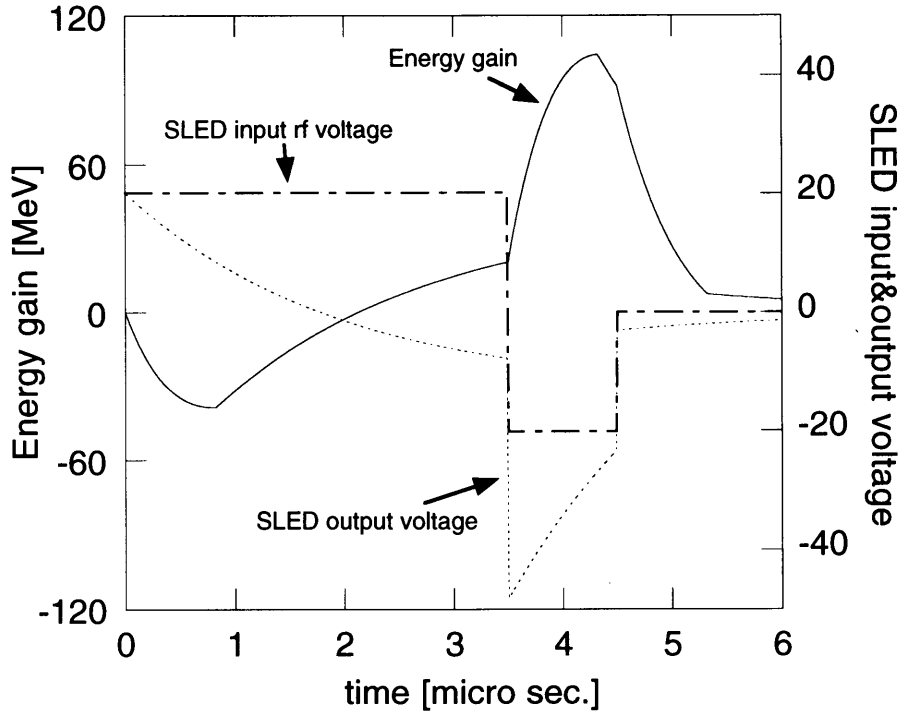

Figure 2.1: Principle of operation with SLED cavity: The rf vector of klystron output, the input rf voltage to accelerating structure and the energy gain in the accelerating structure.

are used to get high peak power. The original SLED scheme has been used at SLAC for SLC linac operation. In the SLED pulse compression system, klystron output power is once stored in SLED cavity. After a few micro seconds the phase of klystron output is flipped by π, the radiated stored rf power from SLED cavity and the reflected klystron output power at SLED cavity which transmit to accelerating structure. Figure 2.1 shows the principle of operation with SLED cavity elsewhere in detail.

In the linac of the KEK JLC design, the bunch train is 85 bunches of 7.2×10^9 electrons/bunch and 1.4 ns bunch spacing. In the linac the energy gain of successive bunches drops due to beam loading. In high frequency linac like X-band, the energy compensation by variety injection timing will be adopted, because the filling time of the accelerating structure is comparable or longer than beam pulse length and the rectangular rf pulse can be obtain by using DLDS and SLED-II rf compression system. In S-band linac of future linear collider, SLED pulse compression system will be used, if new compression system for S-band linac is not developed. As the pulse length of multi-bunch beam is shorter than the filling time of structure, beam loading

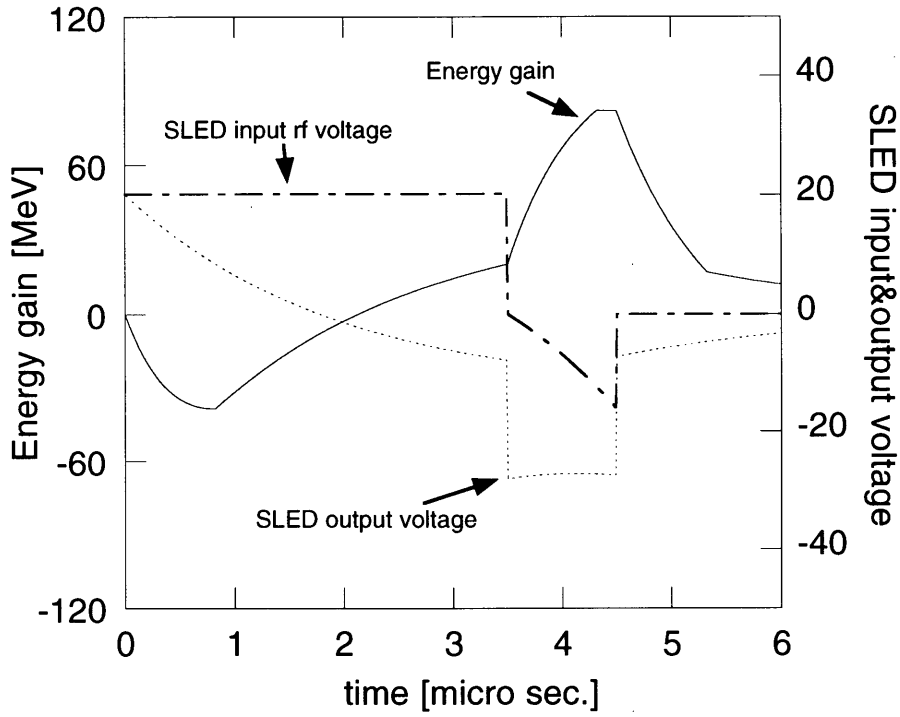

Figure 2.2: Principle of operation with SLED cavity: The rf phase of klystron output are gradually changed after 3 μs. The flat input rf voltage to accelerating structure are generated. The energy gain in the accelerating structure with flat pulse is shown as function of time.

voltage is approximately linear due to the transient beam loading. In this case, the timing energy compensation using flat rf pulse does not have an advantage, because the accelerating efficiency is poor and a compressed energy spread will be limit to the some range. Figure 2.2 shows the generated flat-pulse with SLED system, the peak energy gain is about 20% lower than the normal operation with the phase flip by π (shown in Figure 2.1).

There are some possible energy compensation methods in the S-band linac with or without SLED-I system which are considered and studied at many accelerator laboratories around the world, as follows

1. A chicane is made with four dipole magnets. When multi-bunch beam go through this chicane, the pass lengths of bunches having different energy are different and each bunches are accelerated on the different rf phase in downstream accelerating structure. As the result, multi-bunch energy spread is compressed.

2. Two (or more) accelerating structure running at slightly higher and

lower than fundamental accelerating frequency. In these structures the successive bunches in a train are accelerated with different phase roughly in 90 degrees out of phase from the acceleration. The energy gain of successive bunches increase due to a different phase acceleration. We call this compensation method the ΔF method.

3. Timing energy compensation which is to inject a beam before an rf pulse has filled in an accelerating structure. We call this compensation method to the simple ΔT method.

4. The amplitude modulation method which change the input rf waveform to accelerating structures using some technique and the energy gain of multi-bunch is compensated by the different acceleration due to the modulated rf in an accelerating structure. With SLED system, one is that rf phase of klystron output is reversed three times. The multi-bunch energy is controlled by the timing of the second and third phase reverse [36]. As similar method, after the first klystron phase reverse, either amplitude or phase of klystron output pulse is modulated after the beam injection [37]. Without SLED system, the rf phase is ramped during rf traveling the structure and a beam is switched on after rf-wave reach to the structure output [37].

The compensation method using four dipole magnets is not applicable in linear collider except the injector linac for the damping ring. Because a bunch spacing of multi-bunch beam is changed using this method. In the following, we explain about reliable candidate of energy compensation method in the S-band linac of future linear colliders.

2.2 Energy compensation of multi-bunch beam

2.2.1 ΔF energy compensation method

The $\pm\Delta F$ compensation method compensates the multi-bunch energy spread by keeping a bunch spacing synchronized with an rf frequency. In this compensation method, compensating structures are installed between the regular accelerating structures. When a bunch train goes through the compensating structures driven at an rf frequency which is slightly higher and lower than the fundamental accelerating frequency, successive bunches of the train ride on different phase of the accelerating field (Figure. 2.3). Due to this phase difference, the energy gain of the successive bunches are different. As the result, the multi-bunch energy spread is compressed to a small value.

The compensating voltage $V_b(t)$ in $\pm\Delta F$ compensation sections operating at two different cases of ΔF are plotted in Figure 2.4. The phase difference

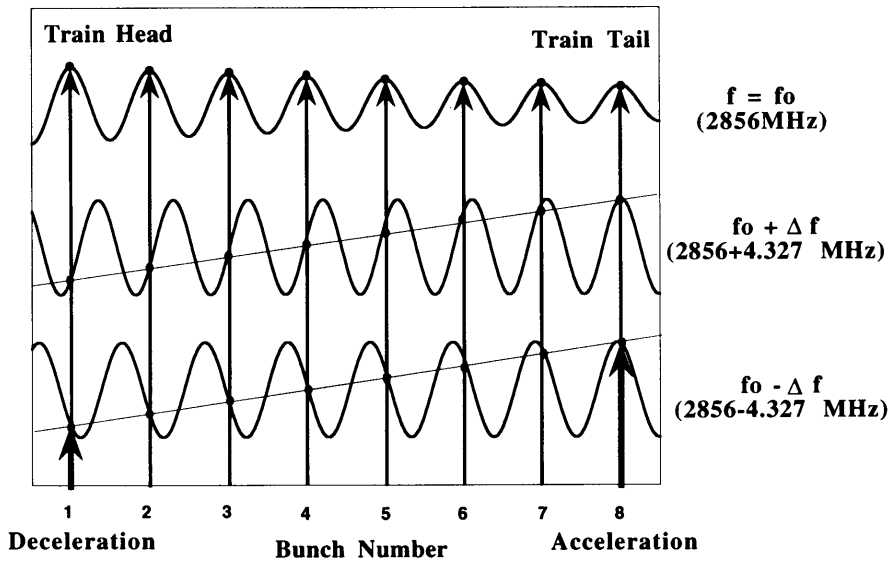

Figure 2.3: Principle of ΔF beam loading compensation

between the first bunch and the last bunch ($\Delta\phi$) is proportional to ΔF (Eq. 2.1) and ΔV_{comp} / $V_{acc,peak}$ (Eq. 2.2).

$$\Delta\phi \propto \Delta F \tag{2.1}$$

$$\Delta F \propto \frac{\Delta V_{comp}}{V_{acc.peak}} \tag{2.2}$$

Small ΔF compensation system needs large accelerating gradient ($V_{acc,peak}$) and the power for the compensation section is proportional to $1/\Delta F^2$. In order to save power, it is desirable to use a large ΔF. However, the final compressed energy spread (ΔE_{final}) is proportional to square of ΔF, assuming linear beam loading voltage within the beam time (Eq. 2.3). The ΔF should be a sub-harmonic of the acceleration frequency to simplify the timing system.

$$\frac{\Delta E_{final}}{E} \propto \Delta F^2 \tag{2.3}$$

When a bunch in a train enters the compensating structures of $\pm\Delta F$, the energy gain is different with bunch head and bunch tail due to the fact that each bunch is accelerated at positive and negative slope of the part of sinusoidal wave in the structures. Two frequencies $F_0 + \Delta F$, $F_0 - \Delta F$

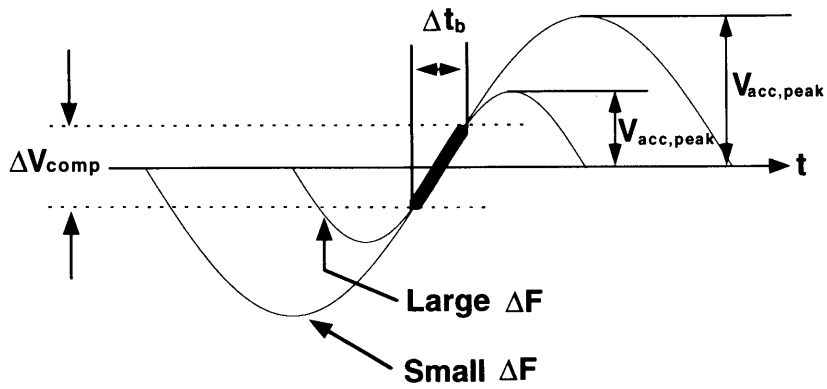

Figure 2.4: The compensating voltage $V_b(t)$ in $\pm\Delta F$ compensation sections operating at a frequency $F_0 \pm \Delta F$

are compensated single-bunch energy spread in first order by a negative and positive rf slope. Therefore, the $\pm\Delta F$ compensating system is consist of the regular accelerating structures and two compensating structures($+\Delta F$ and $-\Delta F$ structure), we call this set of structures the ΔF module.

The ΔF compensation method has a high flexibility for bunch population changes, the amount of compensation can be controlled by the input rf power applied to the compensating structure. The many compensating structure are needed for high beam current, because the input rf power for a compensating structures is limited. As a result, in the case of many installation of the compensating structure, the average accelerating gradient decrease along the linac.

For instance in the different case of ΔF ECS module in S-band linac, Figure 2.5 shows the ΔF ECS modules of the two different cases. One ΔF ECS module has 4 regular accelerating structures and 2 ΔF ECS structures which we call the 1-2-1 ΔF module, another has 8 regular accelerating structures and 2 ΔF ECS structures which we call the 2-4-2 ΔF module. Suppose that in the regular rf unit, the rf pulse width of klystron output is 4.5 μs, the compressed pulse width is 1.0 μs and rf power is fed to the 2 accelerating structures, the rf pulse waveform for the ECS structures is rectangular with a width of 1.0 μs. The output peak power of all klystrons is 60 MW and the filling time of accelerating structure is 830 ns. Figure 2.6 shows the calculation results which are the compensated energy spread of multi-bunch beam and the average energy gain in the ECS module (total energy gain per module/module length) with different module size.

The generated beam loading voltage in the compensating structure is different from in the regular accelerating, because the successive bunches ob-

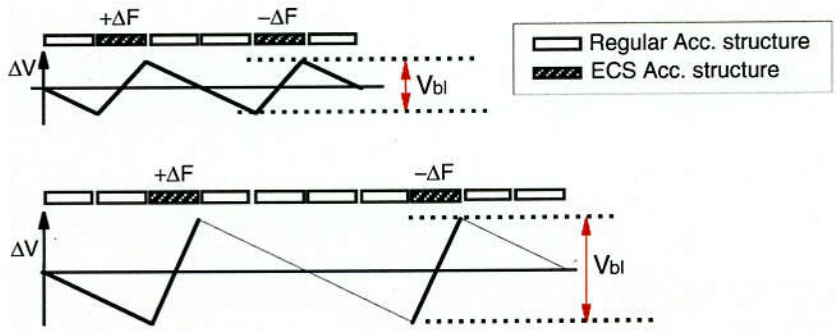

Figure 2.5: Two different size module for ΔF ECS which are 1-2-1, 2-4-2 ΔF ECS modules and the energy difference between first and last bunch in a train.

tain the exited field of different phase by leading bunch. Figure 2.7 shows the beam loading voltage in the regular and ΔF structure. We assumed the parameters of the compensating structure except the fundamental accelerating frequency are same with regular accelerating structure. In Figure 2.6, this effect appears as the different slope of compensated energy spread.

As shown in Figure 2.5, the maximum energy spread of multi-bunch beam in a ΔF ECS module ($V_{bl}/2$) is proportional to the module size and the averaged accelerating gradient in a ΔF module is also proportional to the module size. The relative energy spread ($\Delta E_{mod}/E_{tot}$) turn into small along the linac, where ΔE_{mod} is maximum energy spread in a ΔF module. So it is important to minimize the emittance growth due to chromatic effects at low energy part.

2.2.2 $\Delta\phi$-A energy compensation method

The most simple compensation of the beam loading in ΔT method can be done by injecting the beam before the rf pulse has filled the accelerating structure. The way that the ΔT compensation principle works is shown in Figure 2.8, in which the optimum injection timing is determined by the slope of the beam loading voltage $V_{bl}(t)$ and the voltage $V(t)$ produced by rf pulse . In this simple early injection method with square rf pulse, the beam current at which the energy compensation acts effectively is limited to some range.

We apply thus the amplitude modulation on the input rf pulse for the pulse compression. Using the SLED-I system [38], we can obtain the desirable slope of unloaded voltage by changing input rf waveform for SLED cavities. As discussed in Ref. [34], it is difficult to modulate the input rf to SLED cavity stably using only one klystron. The klystron should not be saturated for the direct amplitude modulation of klystron drive rf, it will enhance the amplitude jitter of klystron output. For a stable operation, a klystron usually

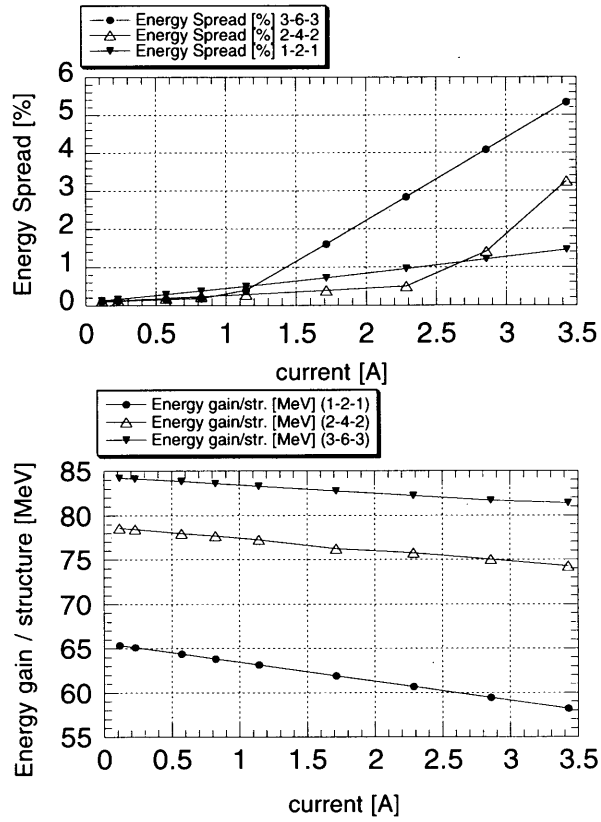

Figure 2.6: The different size module for ΔF ECS which are 1-2-1, 2-4-2 and 3-6-6 ΔF ECS modules. Upper figure shows the compensated energy spread vs. the continuous beam current. Lower figure shows the averaged energy gain vs. beam current.

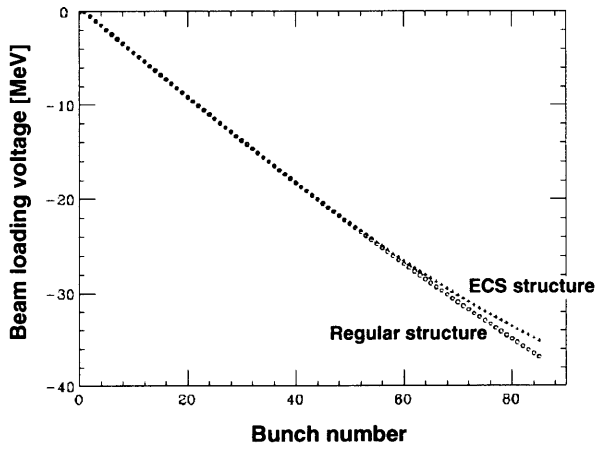

Figure 2.7: The beam loading voltage in the regular accelerating structure and ECS structure.

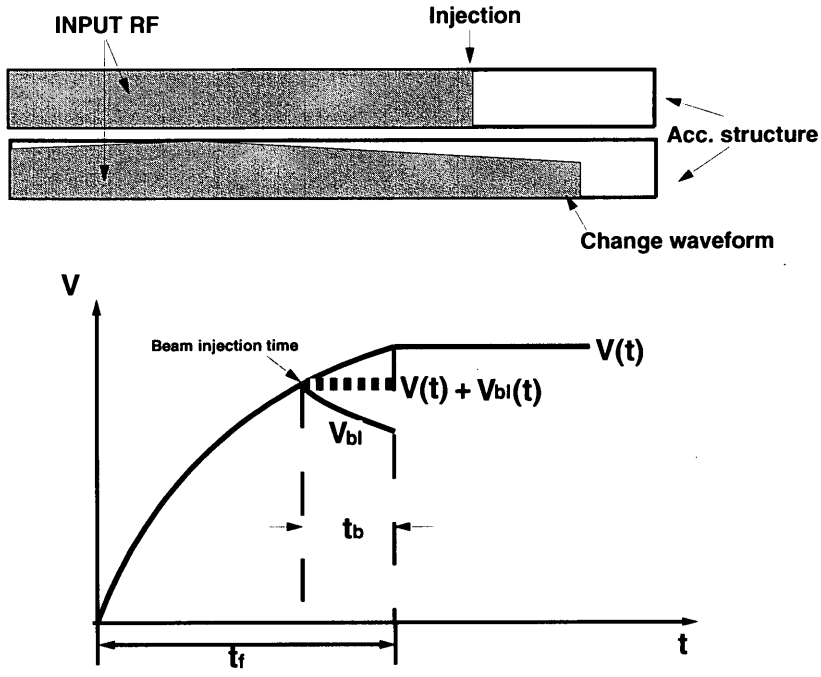

Figure 2.8: Principle of the timing energy compensation (ΔT)

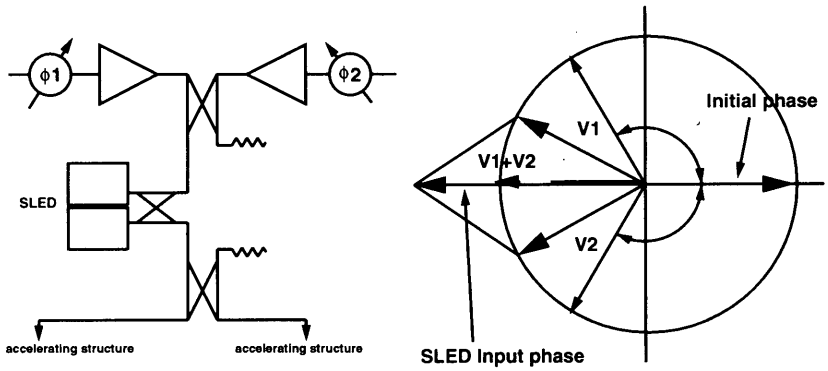

Figure 2.9: Principle of phase modulation to amplitude modulation using two klystrons. [35]

needs to be used in the saturation condition. Thus, modulating the drive rf phase of klystron would be a better method. When the input rf phase for SLED cavity is modulated using only one klystron, the amplitude of output pulse from SLED is modulated. However, in this case a beam acceleration phase changes in the structure. To modulate the amplitude of rf pulse for the SLED cavities at constant phase, two klystrons are needed. Two klystrons run in saturation, keeping the input rf level constant. We control their phases and combine the rf power from two klystrons using a 3 dB hybrid combiner.

Figure 2.9 shows a scheme in which the rf phases of two klystrons are rotated into opposite directions relative to each other. The sum of two phase modulated rf makes amplitude modulated rf with constant phase, which is fed into the SLED cavities. The rest of rf power with different phase go to dummy load (shown in Figure 2.9). The phase modulation of the two klystrons effectively realizes amplitude modulation using this method ($\Delta\phi$-A method).

If bunch population of each bunch is not uniform, the energy of beam does not drop linearly with time. Even in this case, phase modulation to amplitude modulation ($\Delta\phi$-A) method can properly compensate it by changing the speed of phase rotation.

3 Simulation Study

In this section, we carry out the tracking simulation to study the relation between the energy compensation method of multi-bunch beam and emittance growth in the linacs. The multi-bunch energy compensation method can be distinguished in to the two different types of methods which are local and unlocal energy compensation methods. For example the $\Delta\phi$-A method which compensates an multi-bunch energy spread in every accelerating structure is a local compensation, while ΔF method compensates it through several quadrupoles in average, therefore this is an unlocal compensation method. In the case of unlocal compensation, when the multi-bunch beam goes through the some accelerating structures in the linac, the beam has the bunch-to-bunch energy spread due to beam loading. Since bunches with different energies obtain different kick angle at the quadrupole magnets, the trajectories of bunches with different energy are different and eventually cause an emittance growth in the multi-bunch beam. This effect is connected to alignment tolerance of quadrupole magnets.

We study about the dependence of the multi-bunch transverse motion on their energy spread in the case of both the local and unlocal energy compensation. Especially this is important in the low energy part of future linear colliders and this results will guide a choice of energy compensation method in the low energy part.

3.1 Emittance Preservation

In ideal linacs, the normalized transverse emittance is preserved. In the real linacs, the beam has some energy spread and the alignment of components respect to ideal orbit is not perfect. During the beam go through the linac, the emittance dilution occurs due to some effects to the transverse motion. The main sources of the transverse emittance growth are as follows:

1. When the charged particle traverses in an accelerating structure, the wake fields are excited. The following particle is transversely kicked in the direction of the offset respect to the structure axis by dipole-mode wake field which is induced by leading particles. The amplitude of this dipole-mode wake field is proportional to the transverse position and charge of leading particles. By this transverse kick, the trajectories of following particles at different longitudinal positions changes. Finally the normalized transverse emittance increases. In this paper, we call this effect the wakefield effect.

2. The real bunched beam consists of particles having different energies. The particles having different energies obtain the different kick angle in the magnetic field. This effect leads to the different trajectories for

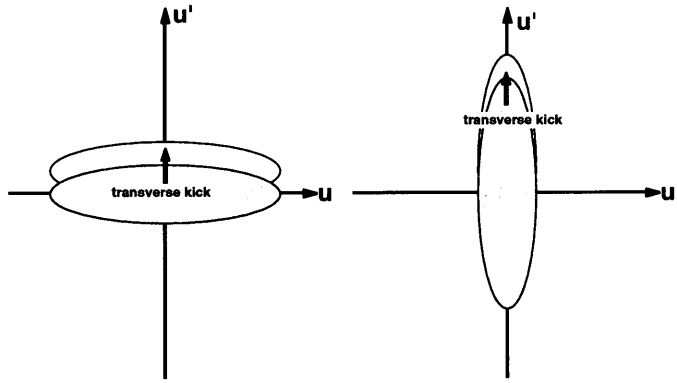

Figure 3.1: Transverse kick due to the dipole-mode wake field in the accelerating structure on the transverse phase space (left:the case of large beta function right:the case of the small beta function)

the particles with different energies. In the betatron oscillation, this effect leads to different phase advances for the particles with different energies. If beam particles having different energies are injected at the off-center of quadrupole magnets, they will differently rotate in the phase space (shown in Figure 3.2). In this paper, we call this effect the chromatic effect.

The wakefield effect depends on the type and the misalignment of the accelerating structures. Recently a variety of structures have been developed to control or damp the long-range transverse wake field for the future linear colliders, the detuned structure [27], the damped detuned structure [28], the choke mode (Shintake type choke mode) structure [29], for example. Multi-bunch instability can be controlled or does not occur using these structures. However, the single bunch instability due to the short range wake field is connected to the iris size of the accelerating structures. For higher frequency band linac, alignment tolerance of the accelerating structures and straightness tolerance for a structure will be tighter to suppress this instability.

On the other hand, the chromatic effect depends on the single and multi-bunch energy spread and the misalignment of quadrupole magnets in the linac. The single bunch energy spread can be controlled by adjusting the accelerating phase in the linac. In multi-bunch operation, the beam has the multi-bunch energy spread due to the beam loading in the accelerating structure. If this energy spread is not compensated completely, the transverse emittance increases due to the chromatic effect. Therefore there is a strong relation between the energy compensation of multi-bunch beam and the emittance growth due to the chromatic effect. In this section, we will study the emittance growth due to misalignment of quadrupole magnets, and

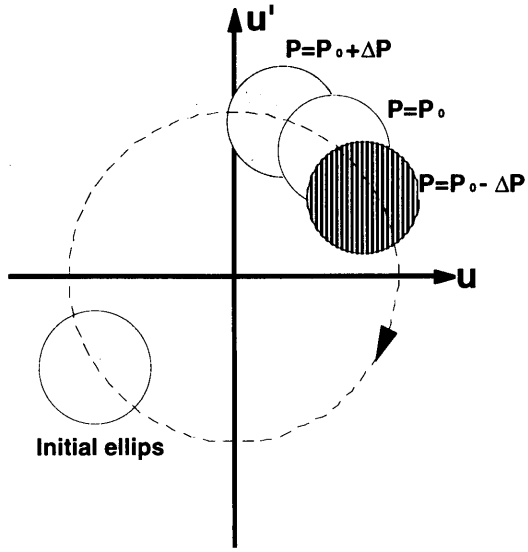

Figure 3.2: Different rotation due chromaticity effect at the magnets on the normalized transverse phase space

compare the cases of local and unlocal compensation methods of multi-bunch beam.

The pulse-to-pulse beam position jitter also introduces the beam offset at the interaction point and luminosity will decrease. Beam quality that takes the pulse-to-pulse position jitter into account is measured with respect to the coordinates of machine axis , and it is expressed as

$$\epsilon_{\text{eff}} = \sqrt{< x^2 >< x'^2 > - < xx' >^2}, \tag{3.1}$$

where x and x' are transverse position and angle. The symbol $\langle\ \rangle$ means the average of all particles in many pulses. Let us call this "effective emittance".

The emittance is measured with respect to the coordinates of multi-bunch weight center, and it is defined as

$$\epsilon_{\text{c}} = \sqrt{< (x- < x >)^2 >< (x'- < x' >)^2 > -(< xx' > - < x >< x' >)^2}, \tag{3.2}$$

where the symbol $\langle\ \rangle$ means the average of all particles in a pulse. When the multi-bunch weight center can be controlled to the machine center by orbit correction and so on, this emittance (ϵ_{c}) is the measure of the beam quality. In this paper, the beam emittance is defined as the averaged value of this emittance for many beam pulses.

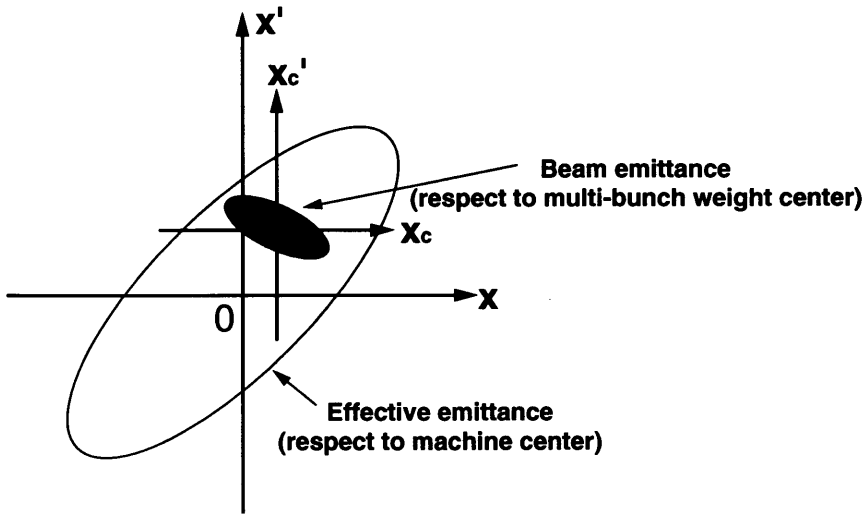

Figure 3.3: Definition of emittance. x is position respect to the machine axis, x_c is position respect to the multi-bunch weight center.

3.1.1 Emittance Growth due to the chromatic effect

In this section, we consider the trajectories of beam particles having different energies in a linac

We consider two particles with different energies in a bunch [24]. The energy of one particle is E_0, another is $(1+\delta)E_0$. When these particles go through the magnets, they get different kick angles in the magnetic fields. We assume that the two particles are injected into a quadrupole magnet having offset x with respect to the magnetic center of the quadrupole and the design energy at this quadrupole magnet is E_0. Here the position difference of two particles at the quadrupole is assumed to be negligible small compared with the offset x. In this case, the difference of transverse kicks of the two particles is given by

$$\Delta x' = \delta k x \tag{3.3}$$

where k is focusing strength of quadrupole magnet. In case that two particle go through the linac, the position difference of two particles at the end of linac is

$$\Delta x_f = \sum_i R_{12}(i)\Delta x'_i = \sum_i R_{12}(i)\delta_i k_i x_i \tag{3.4}$$

where $R_{12}(i)$ is the 1-2 element of transfer matrix from i-th quadrupole to the end of the linac and x_i, k_i and δ_i are the position offset, focusing strength and energy difference at the i-th quadrupole in the linac. Suppose that x_i is randomly distributed along the linac and independent from each other and consider many linacs in the different alignment, average of x_i over the linacs is equal to 0. From Eq. 3.4, we get following relation.

$$< \Delta x_f^2 >= \sum_i R_{12}^2(i)\delta_i^2 k_i^2 x_i^2 \tag{3.5}$$

where $\langle\ \rangle$ means average of many linacs.

Considering that this two particles are contained in a bunch, $< \Delta x_f^2 >/\sigma_{xf}^2$ is equivalent to the emittance growth due to the chromatic effect in the linac, where σ_{xf}^2 is the nominal beam size at the end of linac.

$$\begin{aligned} \frac{< \Delta x_f^2 >}{\sigma_{xf}^2} &= \sum_i R_{12}^2(i)\delta_i^2 k_i^2 x_i^2/\sigma_{xf}^2 \\ &\approx \frac{x_i^2}{2\gamma\varepsilon}\sum_i \gamma_i \delta_i^2 \beta_i k_i^2 \end{aligned} \tag{3.6}$$

where we used the following relation.

$$R_{12}^2(i) = \frac{\gamma_i}{\gamma_f}\beta_i\beta_f sin^2\phi^i \rightarrow \frac{\gamma_i}{2\gamma_f}\beta_i\beta_f \tag{3.7}$$

$$\sigma_{xf}^2 = \varepsilon_f \beta_f \tag{3.8}$$

In Eq. 3.7, γ_i, γ_f, β_i, β_i are Lorentz factor and beta function at the i-th quadrupole and the end of linac, ϕ_i is phase advance from i-th quadrupole and the end of linac, where $\sin^2\phi_i$ is averaged to $1/2$.

In real cases, the difference of offsets of two particles may not be negligible, so the multi-particle tracking simulation is needed to estimate the emittance growth due to chromatic effect. However we can roughly estimate the emittance growth due to the chromatic effect in a linac by replacing from δ_i to energy spread $\Delta E/E$ for single bunch and multi-bunch beam.

3.2 Tracking Simulation

In this section, we study about the multi-bunch emittance growth in the cases of local and unlocal energy compensation using tracking simulation.

This simulation program has been developed for the main linac of future linear colliders and it can simulate the sources of emittance growth [30],

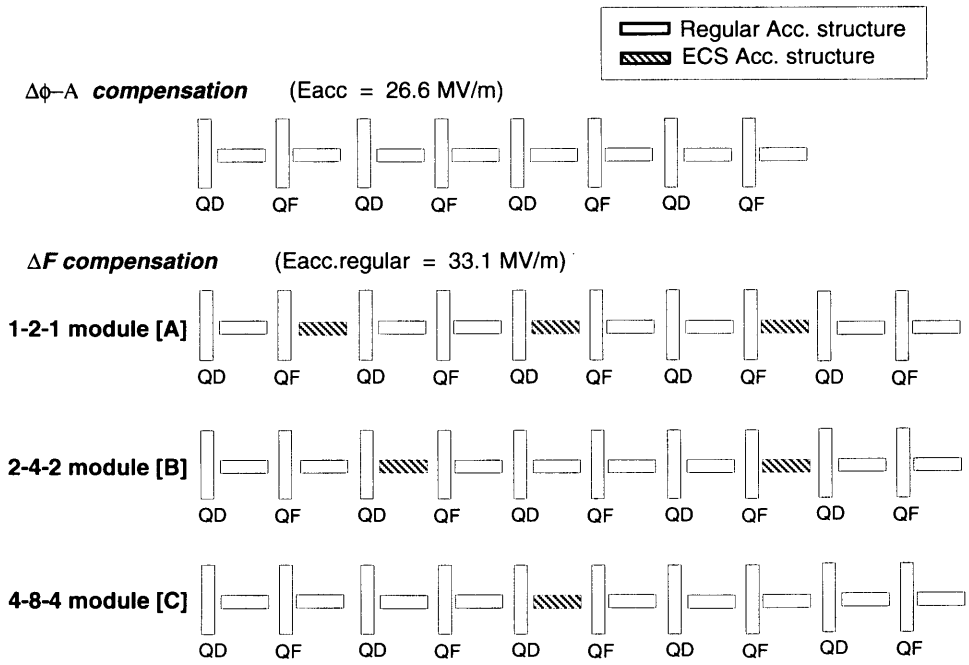

Figure 3.4: The simulated S-band 4-type injector linac. One linac adopted $\Delta\phi$-A ECS, other linacs adopted the three different module size ofΔFECS.

the wakefield effect and chromatic effect due to the injection error and the misalignment of quadrupole magnets and accelerating structures. The wake functions used here are a short-range longitudinal, a short-range and a long-range transverse. Effects of the long range longitudinal wake are taken into account as the different energy gain of different bunches in a train which were calculated using another program. This energy gain includes the beam loading voltage at each structure (Appendix A). In this simulation program, the single bunch and multi-bunch effect can be taken into account and orbit correction also can be simulated.

We carried out simulation with multi-bunch beam to a S-band injector linac where beam is accelerated from 80 MeV to 1.54 GeV. In this simulation study, two types energy compensation methods are adopted to the injector linac, one is $\Delta\phi$-A energy compensation method ($\Delta\phi$-A ECS) which is the local energy compensation method and another one is ΔF energy compensation method (ΔF ECS) which is un-local energy compensation method. Three different module size of ΔF ECS were simulated, which are 4 regular accelerating structures and 2 ECS structures (1-2-1 module [A]), 8 regular and 2 ECS structures (2-4-1 module [B]) and 16 regular and 2 ECS structures (4-8-4 module [C]) (Figure 3.4).

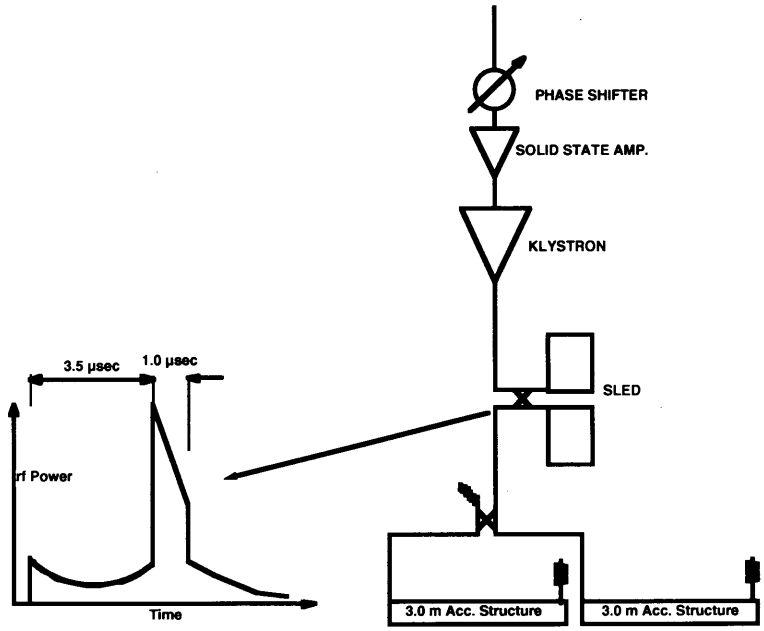

Figure 3.5: Regular rf unit for ΔF ECS method

3.2.1 RF System of Injector Linac

We assume that a regular rf unit of ΔF ECS consists of one klystron, one SLED cavity and two accelerating structures as shown in Figure 3.5, and rf unit of ΔF ECS is composed of one klystron and one ΔF accelerating structure without SLED-I system. In a regular rf unit, a klystron produces an rf pulse with 60 MW of peak power and 4.5 μs of pulse duration. In a regular rf unit of ΔF ECS, at 3.5 μs after the feed of rf pulse into the SLED cavity, the rf phase would be reversed by 180 degrees. The rf power of saw tooth-like waveform is fed into two accelerating structures during 1 μs. The rf pulse waveform for ΔF structures is rectangular with 1 μs width.

An rf unit of $\Delta\phi$-A ECS consists of two klystrons, two SLED cavities and four accelerating structures as shown in Figure 3.6. In rf unit of $\Delta\phi$-A ECS, rf power from two klystrons are combined and divided again to feed into SLED cavities. At 3.5 μs after the rf feed, the phases of two klystrons are rotated into the opposite direction at constant speed. This phase rotating speed is optimized to get flat energy of the multi-bunch beam. In the case of $\Delta\phi$-A ECS, a klystron produces an rf pulse with 60 MW of peak power In this case, the energy gain in $\Delta\phi$-A ECS structure is about 20 % lower than the averaged energy gain in the regular accelerating structure of ΔF ECS.

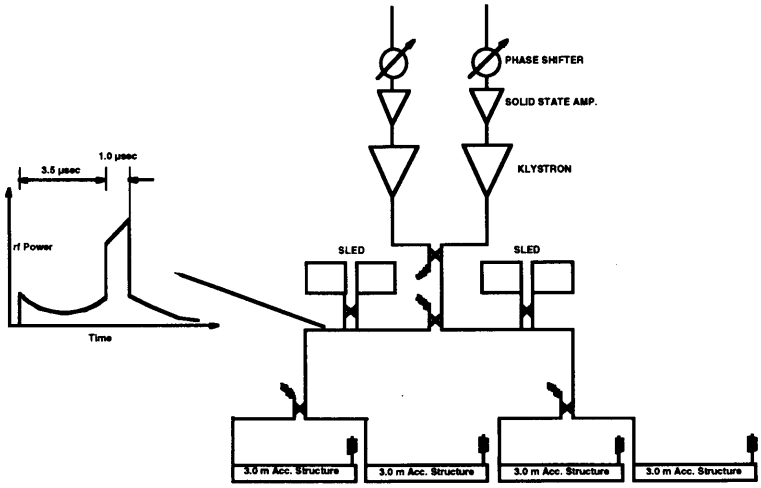

Figure 3.6: Rf unit for $\Delta\phi$-A ECS method

3.2.2 Optics of Injector Linac (ΔF and $\Delta\phi$-A ECS)

The incoming beam has the parameters as shown in Table 3.1.

Table 3.1: In coming beam parameters

Energy (E)	78 MeV ($\gamma = 154$)
α_x,α_y	-1.30
β_x,β_y	3.54 m
$\gamma\epsilon_x$,$\gamma\epsilon_y$	2.3×10^{-4} m
energy spread ($\Delta E/E$)	$\pm$1.53 %
σ_z	1.5 mm

The optical design of the injector linacs are set of simple FODO cells. Cell length of all cases are the same, which don't depend on the choice of the beam-loading compensation method.

Assuming that the β functions in the injector linac varies with design beam energy E as

$$\beta = \beta_0\sqrt{\frac{E}{E_0}}, \tag{3.9}$$

where $\beta_0 = 3.5$ m and E_0=78 MeV, the total phase through the injector linac is

$$\phi = \frac{2\sqrt{E_0}}{\beta_0(dE/ds)}(\sqrt{E} - \sqrt{E_0}). \tag{3.10}$$

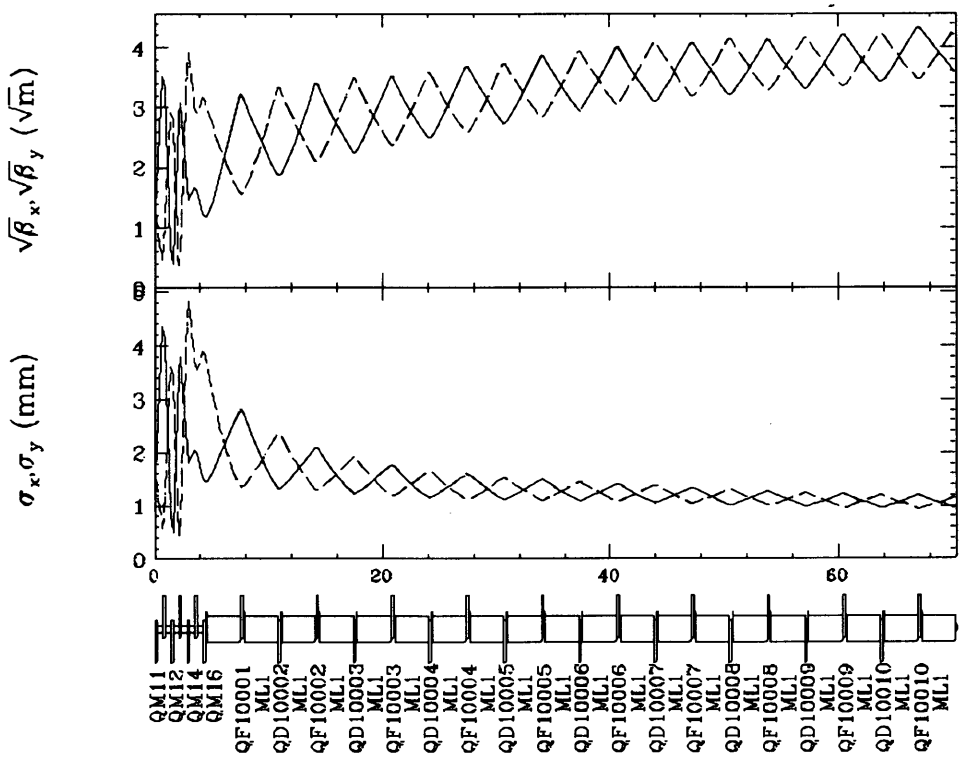

Figure 3.7: Beta functions and beam size for the injector linac which assumes that multi-bunch energy compensation would be adopted with the $\Delta\phi$-A method

In the all cases, the length of the FODO cell is 6.9 m in order to accommodate the 3-m long S-band accelerating structure and the steering magnet for orbit corrections. The quadrupole magnets are 20 cm in length.

The lattice, β functions, and beam size are shown in Figure 3.7 in the case of $\Delta\phi$-A ECS. In this case, the initial horizontal and vertical phase advances per cell are both 90 degrees. Figure 3.8 shows the emittance growth due to misalignment of the quadrupole magnets and the accelerating structures with respect to the beam vs. the initial phase advance per FODO cell, Ψ. Misalignment of the quadrupole magnets and the accelerating structures are assumed to be random as gaussian with r.m.s. 100 μm and 200 μm, respectively. In Figure 3.8, in the low phase advance region we can observe the wakefield effect in the accelerating structures clearly, because the beta function is inverse proportional to phase advance. On the other hand, at high phase advance region the chromatic effect due to single bunch energy spread is dominant. The initial phase advance was set to suppress both the wakefield effect and the chromatic effect.

Figure 3.9 shows the energy spread at the end of linac and the emittance

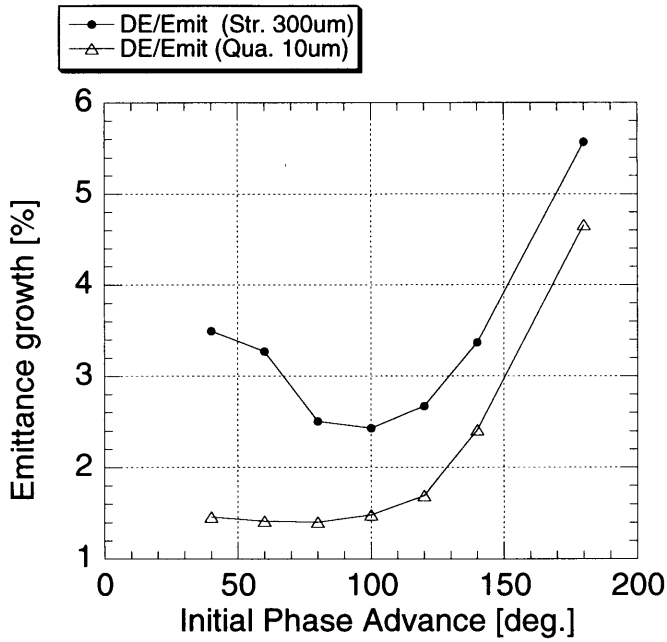

Figure 3.8: The phase advance per cell (Ψ) versus the emittance growth due to the quadrupole magnets and the accelerating structure misalignment with respect to the beam. The quadrupole magnets and the accelerating structures are assumed to have r.m.s. 10 μm and 300 μm misalignment.

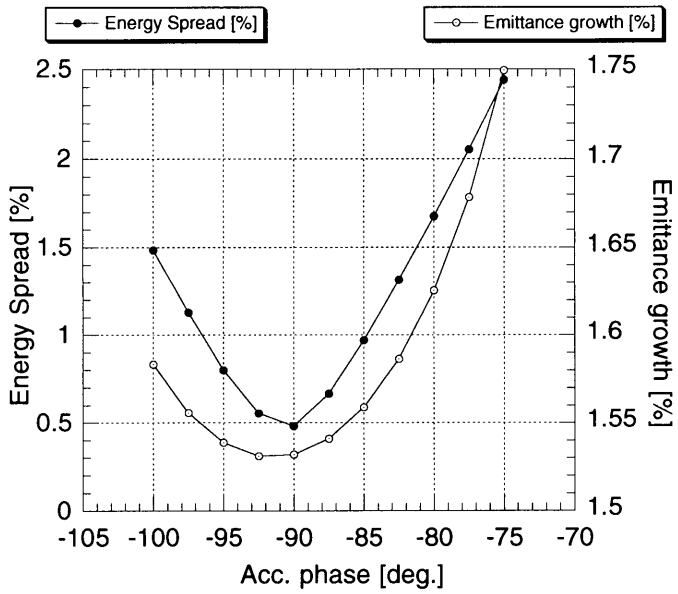

Figure 3.9: The accelerating phase versus the emittance growth and energy spread at the end of linac. The quadrupole magnets and the accelerating structures are assumed to have r.m.s. 100 μm misalignment.

growth with 100 μm misalignment of the quadrupole magnets and accelerating structures vs. the accelerating phase where the -90 degrees correspond to the crest of RF field. From this result the accelerating phase was determined to be -90 degrees (the crest of RF field).

"BNS damping" has been used in linacs [39][40], it is better that the tail part of a bunch should have a slightly lower energy than the head part in order to damp coherent transverse oscillations. The optimum energy difference between the tail part of a bunch and head part roughly estimated to be [24]

$$\Delta E_{BNS}/E = \frac{eQ\beta^2 W(2\sigma_z)}{4E} \tag{3.11}$$

where Q, σ_z, β and $W(2\sigma_z)$ are the charge of bunch, bunch length, the beta function and wakefunction, respectively. In our case, the beta function is proportional to the square root of the energy (Eq. 3.9), and the value of Eq. 3.11 is approximately constant and it is 0.181, assuming Q, σ_z, β_0, E_0 and $W(2\sigma_z)$ were 1.152 nC, 1.5 mm, 3.5 m, 78 MeV and 4×10^{15} V/C/m/m, respectively. This corresponds to 46.1 degrees off phase from the rf crest. It is not acceptable and not realistic because it make a large energy spread and an accelerating efficiency is poor. The rf phase should be decided considering many effects in real linacs.

In the case of ΔF ECS, it is very important to suppress the emittance growth due to the chromatic effect. Especially, in the low-energy part, each

Table 3.2: Parameters of the simulation for the injector linac.

Energy-compensation method	$\Delta\phi$-A method	ΔF method [A/B/C]
Particles/bunch	7.2×10^{9}	7.2×10^{9}
Number of bunches per pulse	85	85
Bunch spacing	1.4 ns	1.4 ns
Incoming emittance;$\gamma\epsilon_y$	2.3×10^{-4}	2.3×10^{-4}
Initial energy spread	1.53 %	1.53 %
Accelerating gradient	26.6 MV/m	33.0 MV/m
Number of structures (ECS structure)	20	24(8)/20(4)/18(2)
Number of Quadrupole magnet	20	24/20/18

section of ΔF should be short, since the relative beam energy spread grows rapidly. This means that many small ΔF sections will be needed there.

In this simulation, all accelerating structures (including the compensating structures) are 3 m, and the length of FODO cell is the same with $\Delta\phi$-A ECS setup. The initial phase advance per cell and accelerating phase was determined to be 100 degrees per cell and -90 degrees from the same consideration as the $\Delta\phi$-A ECS case.

3.2.3 Simulation result

This section presents the results of a simulation of the emittance dilution due to a misalignment of the quadrupole magnets and accelerating structures with an orbit correction using steering magnets. Here, the tracking simulation was performed for only the vertical direction. Since the vertical and horizontal initial Twiss parameters are the same, the alignment tolerance of the components for the vertical and horizontal will be almost the same. Here, the coupling between the horizontal and vertical directions is not considered. The parameters that characterize the condition of the simulation studies are listed in the Table 3.2.

In Figure 3.10, the horizontal axis represents the r.m.s. value of the misalignment of the quadrupole magnet. The misalignment is assumed to have a Gaussian distribution truncated at 3-σ. The vertical axis gives the average of emittance growth ratio over 100 linacs. A 1.53% initial energy spread, and a 100 micron misalignment of accelerating structures with respect to the beam are assumed. We applied a simple orbit correction, which steers the beam to the center of the BPMs. The BPM resolution is assumed to be 10 μm. From this result of the tracking simulation, the ratio of emittance growth in the cases of $\Delta\phi$-A and ΔF are clearly different, the local energy compensation can suppress the emittance growth due to chromatic effect. However the quadrupole misalignment of less than 1000 μm r.m.s. would

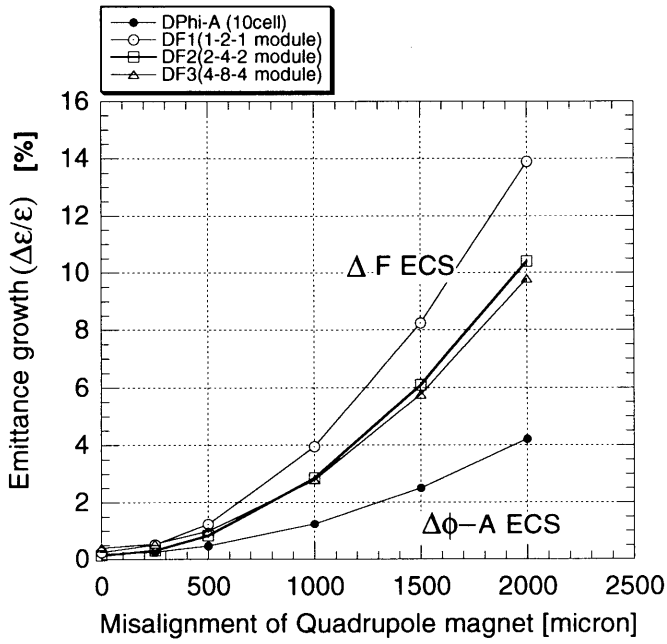

Figure 3.10: Vertical emittance growth, $\Delta\epsilon_y$ / $\Delta\epsilon_{y0}$, as a function of the r.m.s. quadrupole misalignment in the case of $\Delta\phi$-A and the three type ΔF energy-compensation method. (Simulation result of multi-bunch beam)

not cause a serious problem after the simple orbit correction.

We compare this results with the estimation using Eq 3.6. In the estimation, the single bunch energy spread is not considered, but the multi-bunch energy spread due to the long-range longitudinal wakefield is considered. Figure 3.11 shows the calculation result of the estimation, in which the horizontal axis represents r.m.s. misalignment of quadrupole magnets and the vertical axis gives the emittance growth with 4 different type linacs.

The emittance growth is shown in Figure 3.11, which is smaller than the simulation result. This large difference comes from the effect of transverse wakefields, which is not included in the Eq 3.6.

Figure 3.12 shows the simulation result in the case without the wake field except bunch to bunch energy difference. This result agrees with the result of estimation using Eq 3.6 (show in Figure 3.11).

Figure 3.13 shows the result of simulation using only the wake functions of a short-range transverse with single bunch beam.

This result shows the short range wake is dominant for the emittance growth. In the case of ΔF energy compensation the oscillation of transverse motion should increase by the energy spread between head and tail in a single bunch in the accelerating structure, because each bunch is accelerated on the negative and positive sinusoidal slopes of rf-wave in the $\pm\Delta F$ structures.

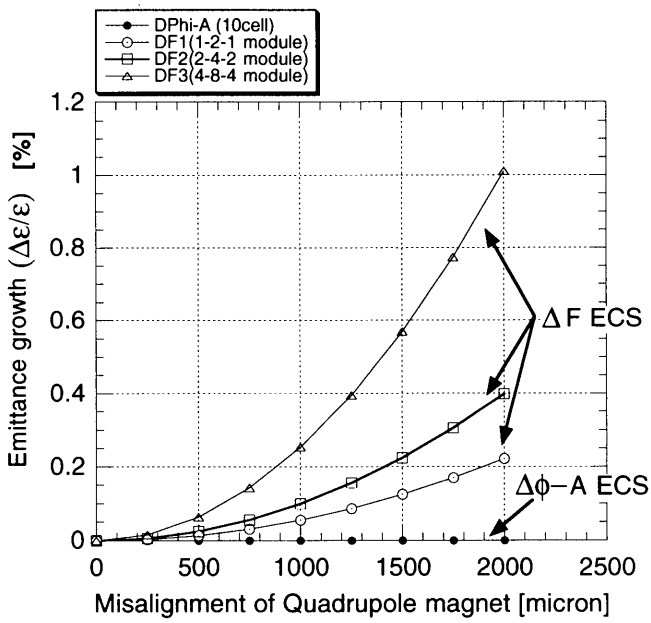

Figure 3.11: The calculation result of the estimation using Eq 3.6. Vertical emittance growth, $\Delta\epsilon_y$ / $\Delta\epsilon_{y0}$, as a function of the r.m.s. quadrupole misalignment in the case of $\Delta\phi$-A and the three type ΔF energy-compensation method.

In the case of $\Delta\phi$-A compensation, since the accelerating phases at every structures are constant, the energy spread between head and tail in a single bunch can be kept at constant in first order.

Figure 3.14 shows the average vertical emittance growth in the injector linac as a function of the misalignment of the accelerating structures. The 10 μm misalignment of BPMs with respect to the quadrupole magnets, a 100 μm misalignment of the quadrupole with respect to the design orbit are assumed. We did not consider any cell-to-cell misalignment within each accelerating structure. We assumed that all accelerating structures have BPMs at structure head, and the accelerating structure was aligned with respect to the beam using the BPMs. In this simulation, we assumed that the alignment of the structure with respect to the beam is determined by the resolution of the BPMs at the structure head. In the real case, an alignment of structure with respect to the beam also depends on the accuracy of attachment error of BPM to structure and fabrication error of BPM. Figure 3.14 shows the results of simulation in which the misalignment of accelerating structure means the alignment error with respect to the beam, not to the design axis. The emittance growth due to a transverse dipole wake-field of the structures for the four different types of linac don't have large difference with simple orbit correction.

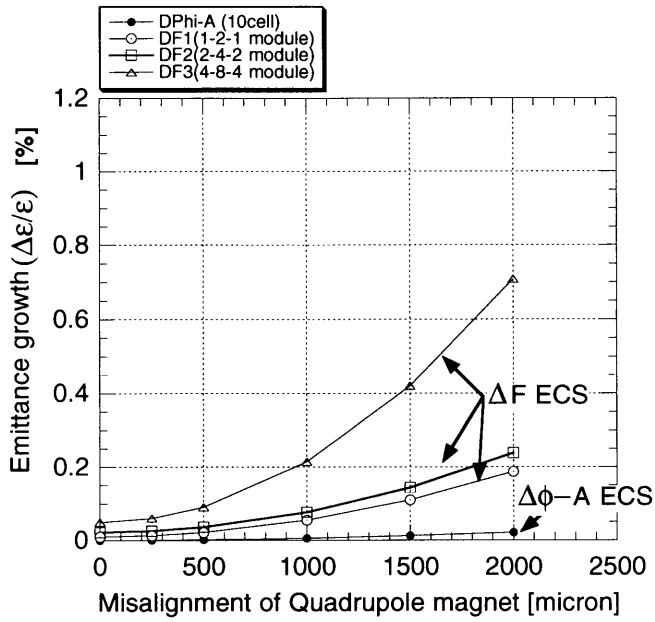

Figure 3.12: Vertical emittance growth, $\Delta\epsilon_y$ / $\Delta\epsilon_{y0}$, as a function of the r.m.s. quadrupole misalignment in the cases of $\Delta\phi$-A and the three types of ΔF energy-compensation method without using the wake functions of a short-range transverse, a long-range transverse and a short-range longitudinal. (Simulation result of multi-bunch beam)

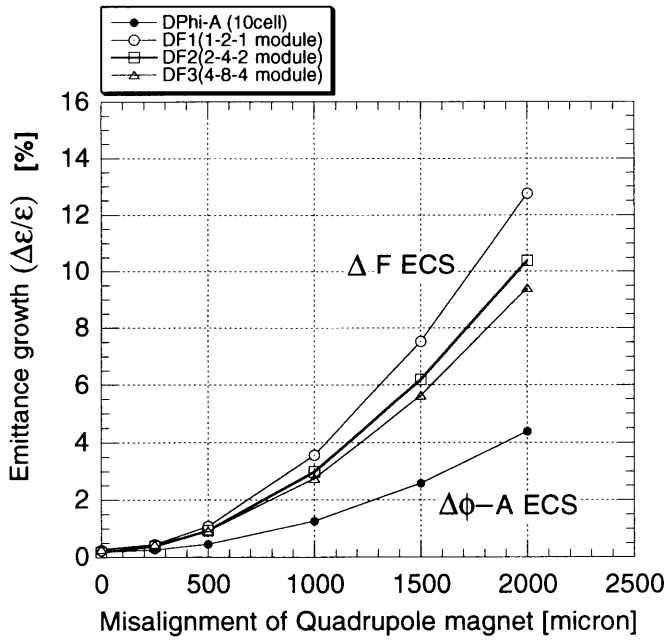

Figure 3.13: Vertical emittance growth of single bunch beam, $\Delta\epsilon_y$ / $\Delta\epsilon_{y0}$, as a function of the r.m.s. quadrupole misalignment in the cases of $\Delta\phi$-A and the three types of ΔF energy-compensation method with using the wake functions of a short-range transverse and a short-range longitudinal. (Simulation result of single bunch beam)

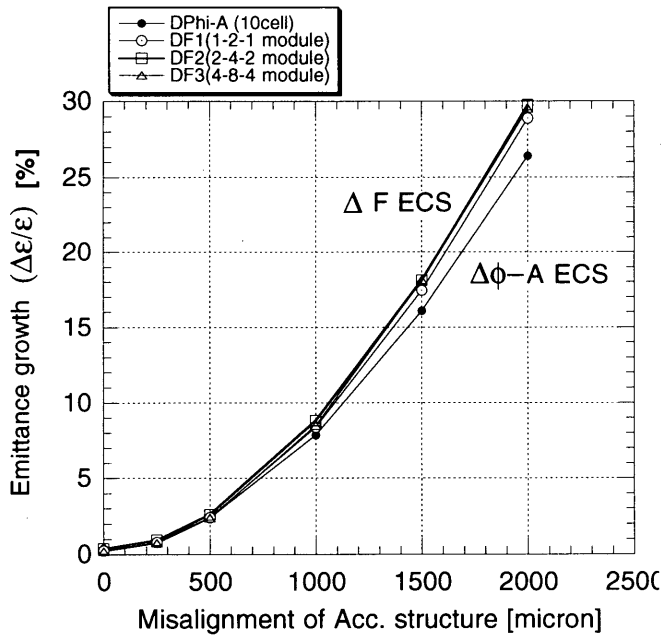

Figure 3.14: Vertical emittance growth, $\Delta\epsilon_y$ / $\Delta\epsilon_{y0}$, as a function of the r.m.s. structure misalignment in the case of $\Delta\phi$-A and the three type ΔF energy-compensation method.

4 Experiments of Energy compensation in ATF

4.1 Experiment of ΔF energy compensation

4.1.1 Experimental Setup

As shown in Figure 4.1, the rf system of the ATF linac consists of 8 regular rf units and 2 ECS rf units. The regular rf unit consists of an E3712 klystron, a pulse modulator, a two-iris SLED cavity [38] [41] , 3 dB hybrid divider, rf waveguides, two 3 m-long accelerating structures and rf dummy loads. The ECS rf unit is composed of a SLAC-5045 klystron, a pulse modulator, and a 3 m-long accelerating structure. The accelerating structures for the energy compensation system are designed for two frequencies ($F_0 \pm \Delta F$). The rf pulse waveform from the two SLAC-5045 klystrons for ECS structures is rectangular with a width of 1.0 μs .

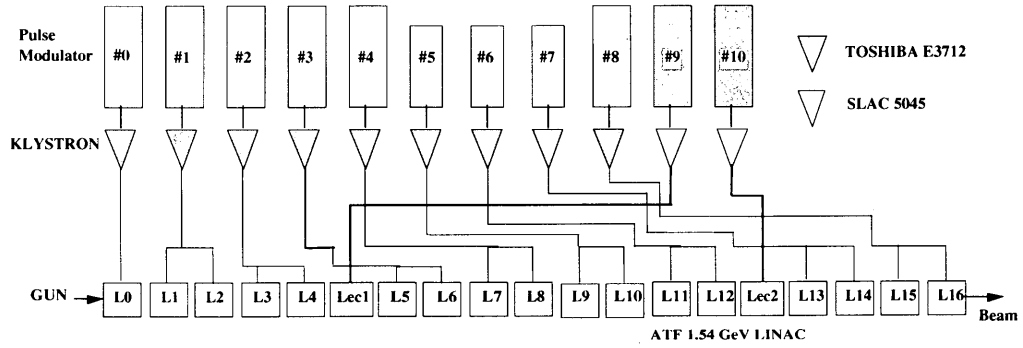

Figure 4.1: The half iris aperture and the group velocity as function of the cell number.

4.1.2 Timing system and sideband signal generation

In the regular accelerating section all bunches are accelerated on the crest of the rf wave, in the compensation section the bunches are on large slope of the rf wave. Even small phase jitter results in large uncertain energy gain of the bunches in the compensating structures, and a very stable accelerating rf signal is required. In the ATF, the rf signal is generated using a 1428 MHz master oscillator, and all necessary frequencies are generated from this reference signal using frequency multipliers and dividers. All the components are synchronized to this master oscillator (shown in Figure 4.2). The sideband frequency for the compensation was selected to be 4.327 MHz, twice the revolution frequency of the DR, and 1/660 of the fundamental accelerating frequency. This frequency was determined by the accelerated bunch number (20 bunches) and the DR revolution frequency [42].

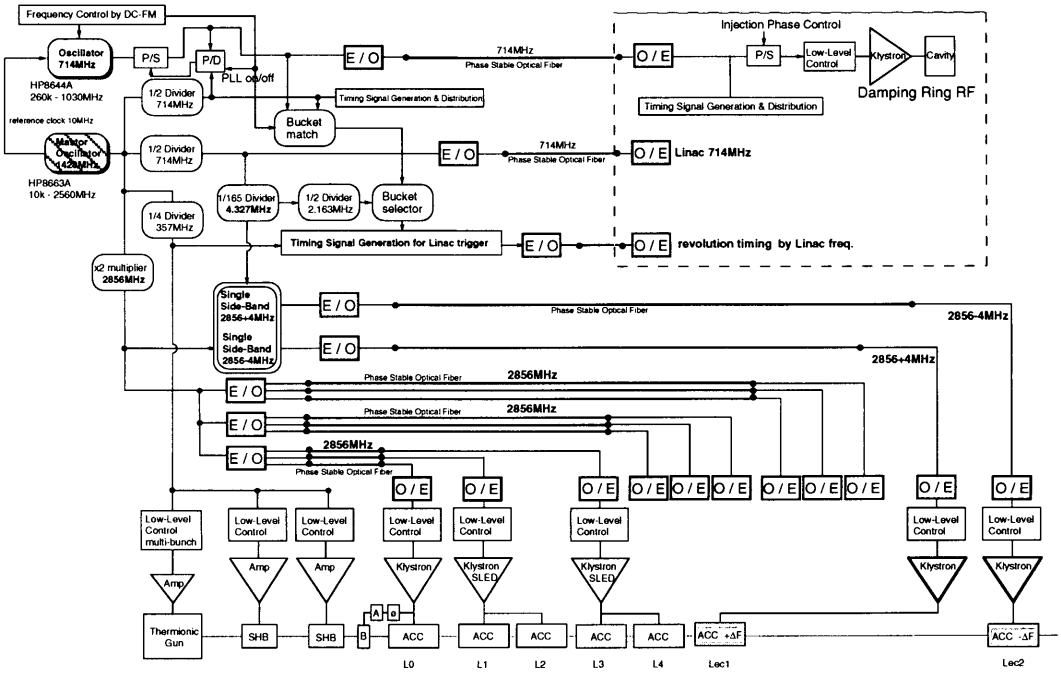

Figure 4.2: Reference signal distribution in ATF

Two compensation signals ($F_0 \pm \Delta F$) are generated by mixing the fundamental (2856 MHz) and the sideband (4.327 MHz) signal in a special module.

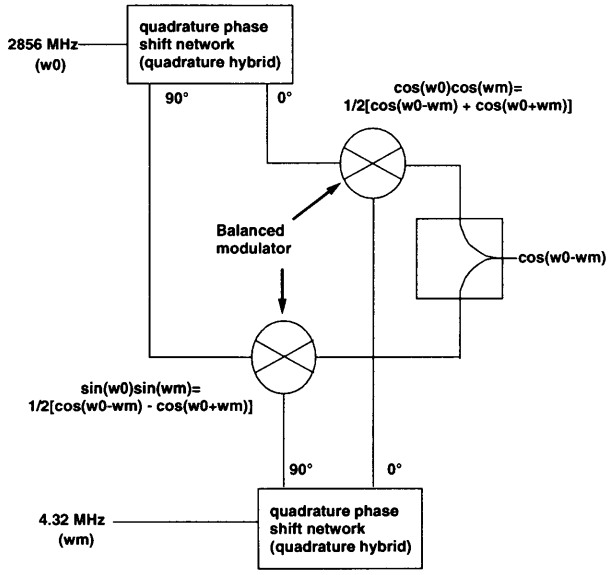

Figure 4.3: Principle of the sideband signal generation

Figure 4.3 shows principle of the sideband signal generation [43]. The fundamental and the sideband signal are first split into two parts that differ 90 degrees in phase and then fed into dual balanced modulators. The output from the modulators is a product of the input signals, which can be expressed as a sum of two sinusoidal signals, with frequencies $F_0 + \Delta F$ and $F_0 - \Delta F$ i.e. the desired sideband frequencies. One of the sideband signals ($F_0 \pm \Delta F$) is in equal and the other is in opposite phase. When they are added in a signal combiner, the sideband with opposite phases cancels out and the only desired sideband remains. By reversing the signals from one of the quadrature phase shifters, both sideband can be generated.

This signal generation method has a further advantage of being feasible with even smaller sideband frequencies, where methods like using bandpass filters become exceedingly difficult. If $\pm\Delta F$ energy compensation method is used with longer pulse trains, a lower sideband frequency is required to keep all the bunches within reasonable linear part of sinusoidal slope.

We further employed a carrier suppression method to reduce the level of the carrier frequency, that inevitably "leak" through the mixers. Pure reference signals could be generated using this method; some results from measurements with a spectrum analyzer can be seen in the Figure 4.4. The unnecessary frequencies are suppressed by -60 dB. In long term tests, due to temperature variations etc., the suppression ratios were found to drift a little but to stay over 50 dB.

Phase jitter was measured by using a mixer. Two signals of the same sideband were generated and feed them into a mixer. The mixer output is promotional to the phase difference between the signals. The result of this measurement was 1.75 degree in FWHM (σ = 0.82 degree) [43].

4.1.3 Measurement system of the beam energy and profile

The beam energy of each bunch was measured from the strength of the bending magnets and a beam position after the bending magnets which are located in the entrance of the beam transport (BT) line (Figure 4.5). The measurement of the beam position for each bunch was performed using strip-line type beam position monitor (BPM) [44]. The energy difference of each bunch in a train was calculated from the horizontal beam position and the dispersion function (η_x) at the BPM.

The multi-bunch beam signal through the long cables was stretched by 850 MHz Gaussian low pass filters to get a wide pulses with good signal to noise ratio (S/N). The stretched beam signal was measured using the digital oscilloscope of real-time 2.5 GHz sample. The position calculation was carried out using:

$$X = k\frac{V_2 - V_4}{V_2 + V_4} \tag{4.1}$$

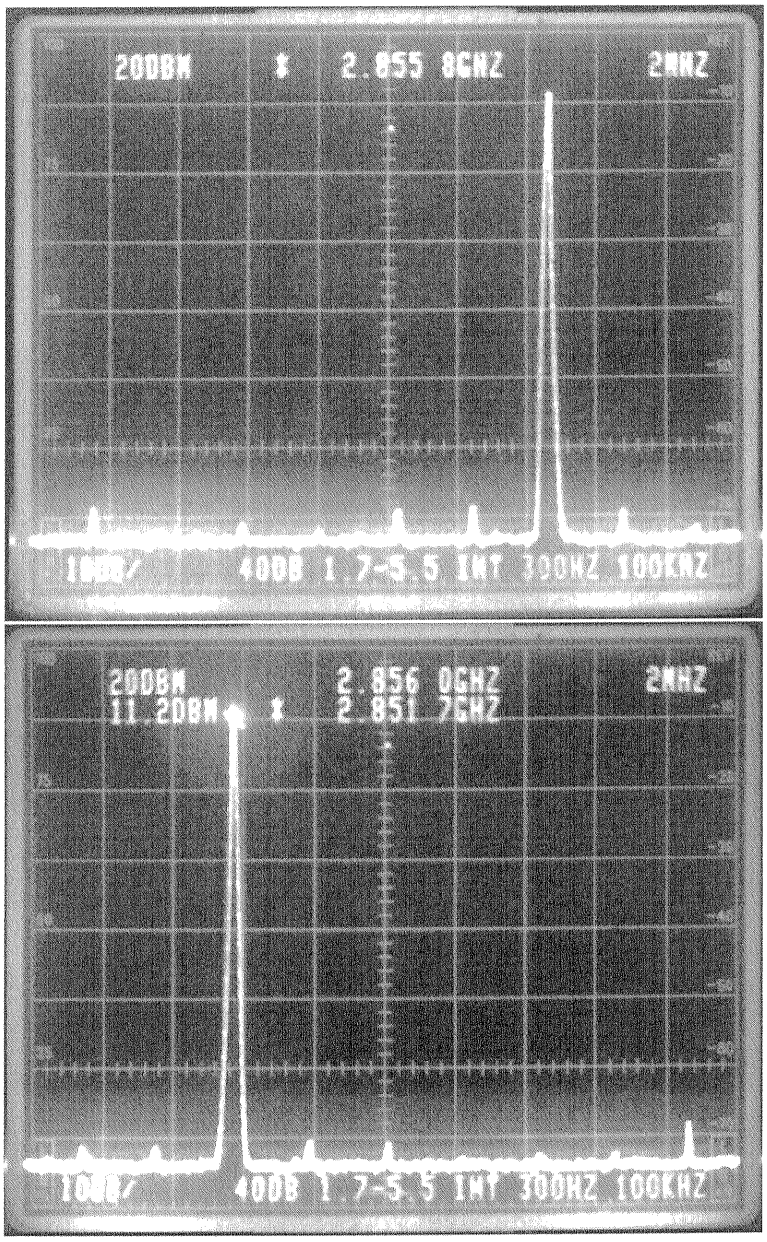

Figure 4.4: Spectrum of the generated sideband signals (Up:upper sideband, Down:lower sideband)

where V_2 and V_4 are the pulse hight of bunch signal from the horizontal electroads and k is a coefficient of position sensitivity. A pulse height of bunch signal was derived by a parabolic curve fitting to sample data.

The limit of position resolution is ordinarily determined by the ratio of an amplitude of signal (S) to its thermal noise (N). In this measurement, the voltage of thermal noise (e_n) was about 2.7×10^{-5} V at the input of the oscilloscope.

$$\begin{aligned} e_n &= \sqrt{4kTBR} \\ &= \sqrt{4 \times 1.38 \times 10^{-23}[J/K] \times 300\ [K] \times 850\ [MHz] \times 50\ [\Omega]} \\ &= 2.7 \times 10^{-5}\ [V] \end{aligned} \tag{4.2}$$

Here k, T, B and R are Boltzmann constant, temperature, band width and impedance of cable, respectively. As the nominal signal height was 500 mV, the S/N was 1.85×10^4 at the input of the oscilloscope , assuming no other noise except thermal noise. The position resolution from S/N and a coefficient of position sensitivity (7200 μ m) was expected to be 0.3 μm which dose not include the thermal noise of oscilloscope [45].

On the other hand, this oscilloscope converts the analog signal using 8-bit analog-to-digital converter (ADC). In case that the amplitude of beam signals are 500 mV and the vertical range is 200 mV/div, a 1-bit quantization error of ADC correspond to 45 μm. This value was larger than the derived resolution from S/N, so the position resolution of the BPM system in this measurement was dominated by the resolution of oscilloscope's ADC. The systematic error of the fitting using parabolic function is smaller than the derived error from the ADC resolution.

Assuming that the error of each sample data is the 1-bit of ADC, the vertical range is 200 mV/div, and the pulse height is 500 mV, the standard deviation σ_V for a pulse height of bunch signal (V) is about 4.2 mV which was derived from the following equation

$$\sigma_V^2 \simeq \sigma_{a_0}^2(\frac{\partial V}{\partial a_0})^2 + \sigma_{a_1}^2(\frac{\partial V}{\partial a_1})^2 + \sigma_{a_2}^2(\frac{\partial V}{\partial a_2})^2 + 2\sigma_{a_0a_1}^2(\frac{\partial V}{\partial a_0})(\frac{\partial V}{\partial a_1})\cdots \tag{4.3}$$

where $\sigma_{a_0}^2, \sigma_{a_1}^2, \sigma_{a_2}^2$ are variances for a_0, a_1, a_2 respectively and $\sigma_{a_0a_1}^2$ is covariance between a_0, a_1. As the beam position is calculated using Eq. 4.1, the error of beam position (σ_X) is given by

$$\sigma_X^2 \simeq \sigma_{V_2}^2(\frac{\partial X}{\partial V_2})^2 + \sigma_{V_4}^2(\frac{\partial X}{\partial V_4})^2 \tag{4.4}$$

where $\sigma_{V_2}^2, \sigma_{V_2}^2$ are the standard deviation for V_2, V_4. We made the assumption that the fluctuations in V_2, V_4 are uncorrelated. In case that BPM's coefficient of position sensitivity is 7200 μm , the pulse height of beam signal from two electrodes are 500 mV and the fluctuations of pulse height are 4.2 mV,

the standard deviation (σ_X) of beam position is estimated to be 40.7 μm. The position resolution (40.7 μm) is converted into the energy resolution of 0.0060 % because η_x is 0.685 m at the BPM. Since this energy resolution is small compared to the DR energy acceptance, this BPM reading system is sufficient to measure the beam position for each bunch.

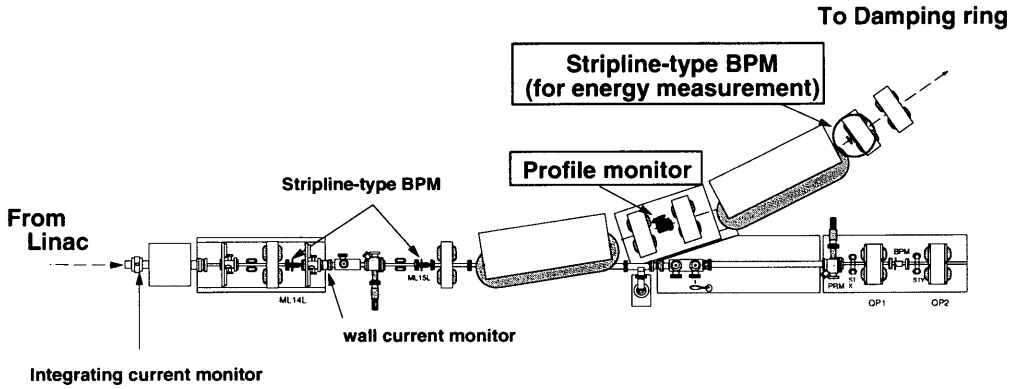

Figure 4.5: Layout of entrance of the beam transport line

The beam profiles were observed by a profile monitor using an optical transition radiation (OTR) [46]. The OTR emitter is made by polished stain less steal which has 1 mm thickness and 1/2 λ flatness ($\lambda = 500\ nm$). The emitted light (OTR) is reflected by a mirror to avoid the x-ray and fed to a fast gated camera which has 3 ns gate width. The video signal of the gate camera is analyzed by a video analyzer using a work station. The analyzer calculates in x and y the fwhm, the peak position, the peak value, etc., in real time. The profile of different bunches were distinguished changing the delay of the gated camera timing with 2.8 ns step. The beam energy spread of each bunch was measured from a horizontal beam size on the OTR monitor at the entrance of BT line.

4.1.4 The beam test of ΔF ECS

Adjustment of the rf phase for the ECS

An adjustment of the rf phase for the ECS structure was performed using the OTR monitor at the entrance of BT line. The gate timing of the OTR camera was set to the center bunch of the bunch train and the output power of each klystron for ECS is set to required value which was derived from beam current. The current of the bending magnet was adjusted that the

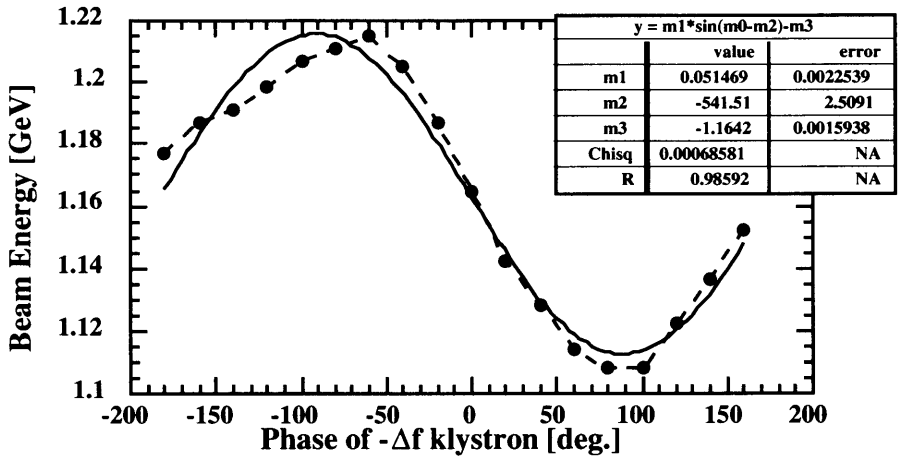

Figure 4.6: ECS phase scan The measurement of multi-bunch energy. The plots are measured beam energy with 20 degree step and the line is fitted sinusoidal function.

bunch profile was seen on the center of the OTR emitter. The rf phase of ECS structure was scanned with 20 degrees step. Each rf phase of the two ECS structures was adjusted individually. Figure 4.6 shows the beam energy dependence on the ECS phase. The optimum phase was determined from the result of the phase scan to find 90 degree apart from the accelerating phase.

The dispersion function measurement

The dispersion function at the BPM was measured by changing the beam energy in the linac and compared to the calculated value by the program 'SAD' [47]. In this dispersion measurement, the changed value of beam energy was evaluated by measuring the intensity peak position of a beam profile on the OTR monitor which located in the entrance of the BT line, then the calculated dispersion function at the OTR monitor was used to derive the energy difference ($\Delta E/E$) form the change of beam position. As a result, the measured dispersion function at the BPM was about 14 % lower than the calculated value.

This difference could have come from: the change of the beam injection orbit into the BT line from the linac due to change of beam energy, an error of the BPM's coefficient of sensitivity, an error of scale factor on the OTR monitor, error of the magnetic field and effective length of the bending magnets. The BPM's coefficient of sensitivity (k) was measured precisely before installation. The error of k value should be comparable with the

fluctuation of measured k value (σ_k) which was 1.1 % for the same type 8 BPMs. The magnetic field of the bending magnets was also measured before installation, therefore the field error should be less than 1% from the systematic error of the measurement. If the beam injection angle into the BT line change 2 mrad, the contribution of this angle error to the dispersion is 1.4 % at the BPM (the calculated value was 0.685 m). It is difficult to calibrate the scale on the OTR emitter, because the scales of the image were different between the near side and the far side of OTR emitter depends on distance from the camera. Another reason is the systematic error of position measurement using OTR monitor due to the change of the beam shape. On the other hand, an accuracy of the calculated η_x depends on the strength, effective length and alignment of magnets. It is expected that the error of the calculated value is smaller than the measurement error of OTR monitor. The dispersion function of calculated value by the program 'SAD' was used in this beam test for the $\pm\Delta$ ECS.

The result of measurement of multi-bunch beam

In this experiment, the multi-bunch of 23 bunches/train accelerated up to 1.16 GeV with intensity of 3.2×10^{10} electrons/train. The bunch population of each bunch is shown in Figure 4.7.

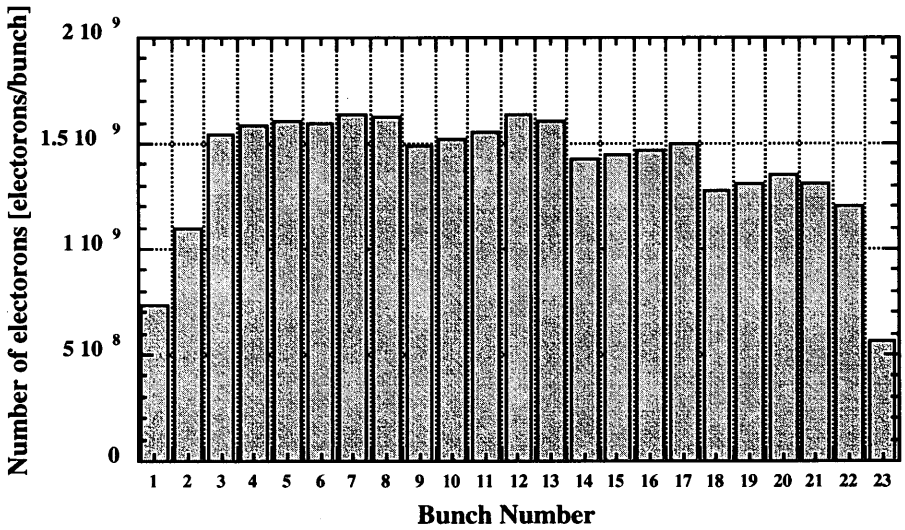

Figure 4.7: Bunch population of the multi-bunch beam

After the adjustments of the ECS rf phase, the rf power of klystrons were

set to get a flat energy distribution for all bunches as 1.9 MW for $+\Delta F$ and 1.5 MW for $-\Delta F$ in this low charge compensation. As a result, the ECS could compress the energy spread of multi-bunch to about 0.5 %. The results of ECS on/off are shown in Figure 4.8. The energy of bunches distributed in about 1.5 % without ECS, where the calculated energy spread was 2.8 %. This difference between the measured and calculated values could have come from the difference of beam injection timing to rf pulse at regular sections. In calculation, we assumed that a first bunch is injected into a structure after rf pulse is completely filled. In this experiment, beam injection timing was not completely adjusted to the above timing. The apparent energy decrease of the head bunches came from a BPM miss-reading caused from the side tail cut by the collimator in front of the BPM.

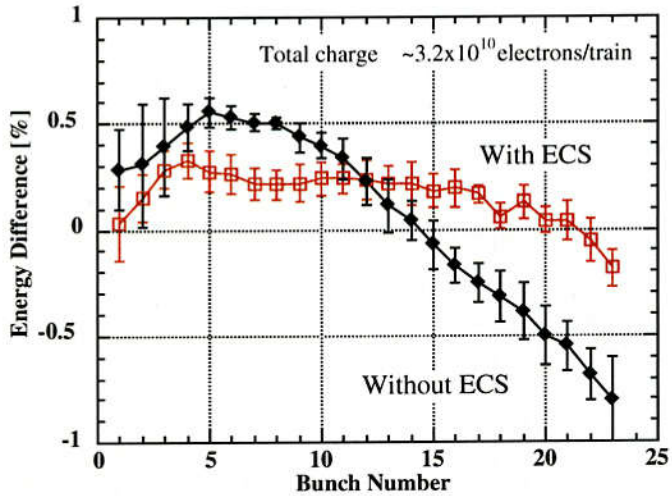

Figure 4.8: The measured multi-bunch energy spread with and without ECS.

Figure 4.9 shows a single-bunch energy spread of each bunch with $\pm\Delta F$ ECS and $+\Delta F$ ECS only. The single-bunch energy spread with the $\pm\Delta F$ was around 0.3 % (FWHM). When only $+\Delta F$ ECS is applied on, the increase of single-bunch energy spread is expected if the compensate voltage is high. In this low compensation voltage, the generated single bunch energy spread in compensating structures was comparable with the generated energy spread in the regular section. Therefore there was no significant difference in this low compensation voltage. The beam test of the ECS was performed using 2856±4.327 MHz structures in the ATF linac. When the measured energy difference was about 1.5 %, the ECS could compress it to 0.5 % by using rf power of with 1.9 MW for $+\Delta F$ and 1.5 MW for $-\Delta F$ with 3.2×10^{10} total intensity. The single-bunch energy spread was less than about 0.5 % at the case of total charge/pulse = 3.2×10^{10}. Clear compensation of single

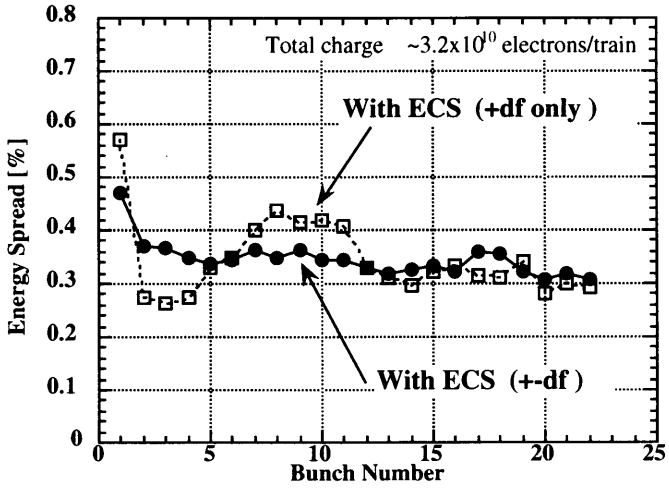

Figure 4.9: The measured single-bunch energy spread with $\pm\Delta F$ and $+\Delta F$ only ECS

bunch energy spread by the effect of a negative and positive slope in the compensating section was not observed in these low compensating voltage.

4.2 Beam test of $\Delta\phi$-A energy compensation

To verify that the $\Delta\phi$-A beam loading compensation scheme works as predicted, we performed preliminary beam test in the ATF injector linac for the damping ring. The ATF S-band linac consists of 80 MeV pre-injector, 8 regular accelerating units, two units of energy compensating structure for ΔF energy compensation. Each regular unit contains SLED-I pulse compression system and the compressed rf power is fed into the two accelerating structures. For this experiment, the first and second regular sections were used and a chicane to measure the multi-bunch energy distribution was constructed downstream of this two regular rf units. ATF linac accelerates a multi-bunch beam that consists of 20 bunches with 2.8 ns spacing.

4.2.1 Experimental setup

We preliminary tested $\Delta\phi$-A method using two-klystron combination, Figure 4.10 shows the rf system of this experiment. It consists of two 85 MW klystron (TOSHIBA 3712), two dual-iris S-band SLED-I cavities [41], 3 dB hybrid combiner, high power wave guides, rf loads and a high power mechanical phase shifter. In this rf set up, rf power from the two klystrons were combined using 3 dB hybrid combiner, after that combined power was divided again to avoid a break-down at SLED cavities. High power mechanical phase shifter was used to adjust the relative phase between two rf units

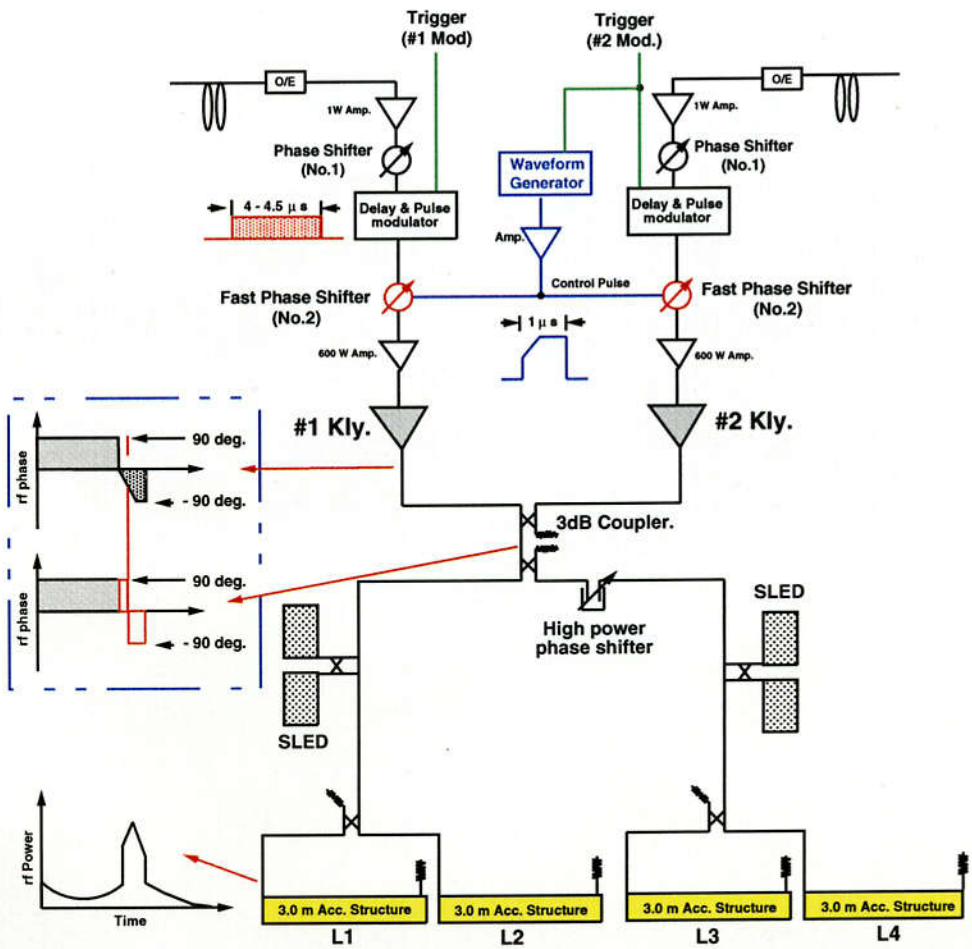

Figure 4.10: Experimental setup for $\Delta\phi$-A beam loading compensation

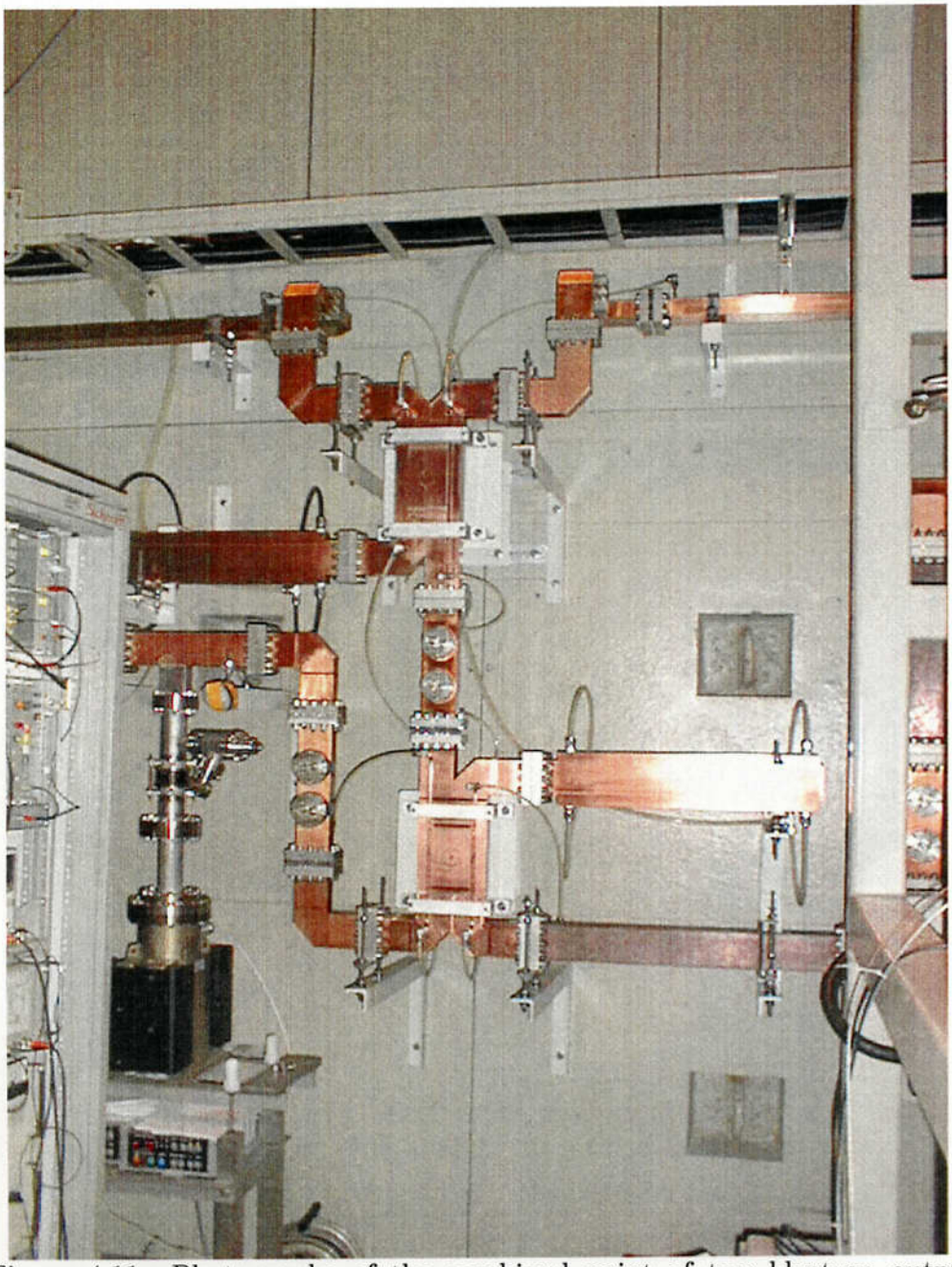

Figure 4.11: Photographs of the combined point of two klystron output power.

(L1,2 and L3,4 structures in Figure 4.10, 4.18). Rf power was measured using -70 dB Bethe-Hole coupler, the rf detector (Appendix B.1) , low pass filter, at several points which were each klystron out, the combined point, input of the SLED cavity and the entrance and exit of the accelerating structure.

In the low level rf circuit, the 2856 MHz phase shifters (No.1) tuned the rf phase of the input CW rf to the beam. By using Delay and Pulse Modulator, the CW rf was modulated into a short pulse with 4.5 μs width and the rf timing to klystron voltage was adjusted. The fast phase shifters (No.2) using varactor diode were used to rotate the drive rf phase of klystron. A control pulse with 1.0 μs width for the fast phase shifters was generated by the arbitrary waveform generator (SONY Tektronix AWG510), and changes the rotating speed of drive phase. In this beam test, rotating speed of rf phase was changed at constant rate as shown in Figure 4.12.

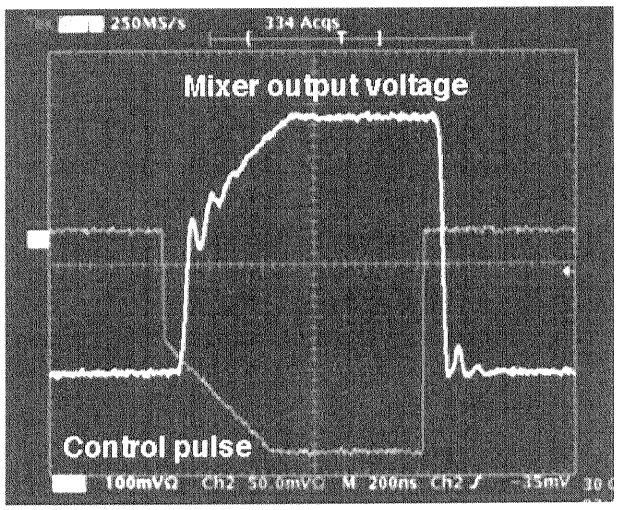

Figure 4.12: The time response of the phase shifter to the control pulse which was measured using a double balanced mixer with the phase rotation speed at 90 degrees/400 ns.

The phase shifters in this experiment for phase rotation of klystron drive rf were the reflection-type phase shifter using varactor diode (Figure 4.13). This type of varactor diode phase shifter is basically analog device in which the varactors function as variable reactance elements. This variable reactance is achieved through voltage-tuned capacitance of the diode under reverse-bias condition, therefore each of the rotating speed is different when the rf phases are rotated into opposite direction. This should be come from the time response of capacitance of the diode.

Recently, an advance of the high speed analog-to degial converters allow the I/Q phase shifter (Figure 4.13) to be implemented digitally. The I/Q phase shifter has some advantage of that it has good linearity and rf phase

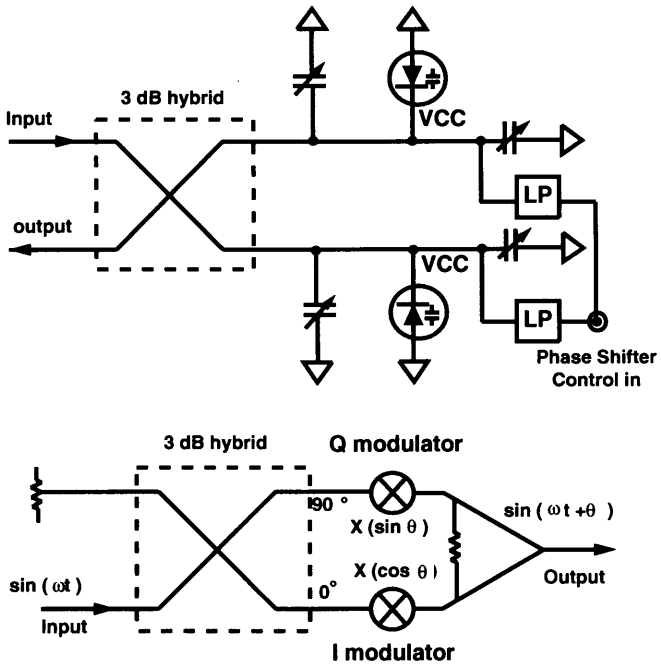

Figure 4.13: The reflection-type phase shifter using varactor diode (up) and I/Q phase shifter (down).

can be controlled continuously. If the I/Q phase shifter is used as the phase shifter for klystron drive rf, the desired phase profile will be generated. The I/Q phase shifter have been used as the phase shifter for klystron drive rf at C-band group in KEK [48] and at NLCTA in SLAC [49].

4.2.2 Rf measurement

The rf waveforms were measured at the several points. Then the low pass filter was used to eliminate the second harmonics from klystron output. Figure 4.14 shows rf waveforms at the input of accelerating structure in the three cases with different rotating speed of klystron rf phase. One is the fast phase reverse in which the phase reversal response time was about 50 ns. The other cases are slow phase rotation, in there cases the phase of klystron drive were changed at speed of 90 degrees/400 ns and 90 degrees/800 ns.

Figure 4.15 shows the measured rf amplitude at the output of klystron, the combined point and the input of accelerating structure (SLED output) in which phase rotation speed was 90 degrees/800 ns. During the phase rotation, we can find the quadrature component of combined rf went through the dummy load (the middle waveform in Figure 4.15).

We measured the rf phase of klystron output and combined point using the phase detector (Appendix B.2). This phase detector decomposes an rf

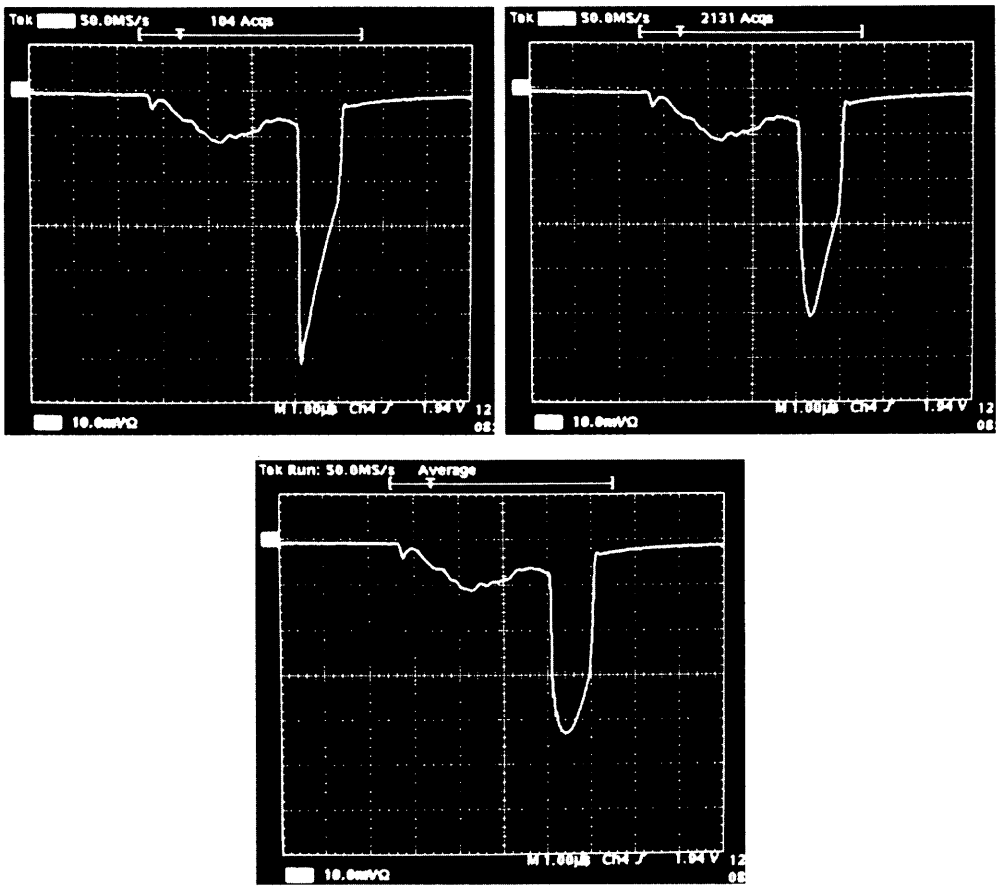

Figure 4.14: Photographs of the rf waveform at the input of accelerating structure (output of SLED cavity). The upper-left is the case of fast phase reverse (50 ns), the upper-right and the lower are the case of slow phase reverse (90 degrees/400 ns and 90 degrees/800 ns).

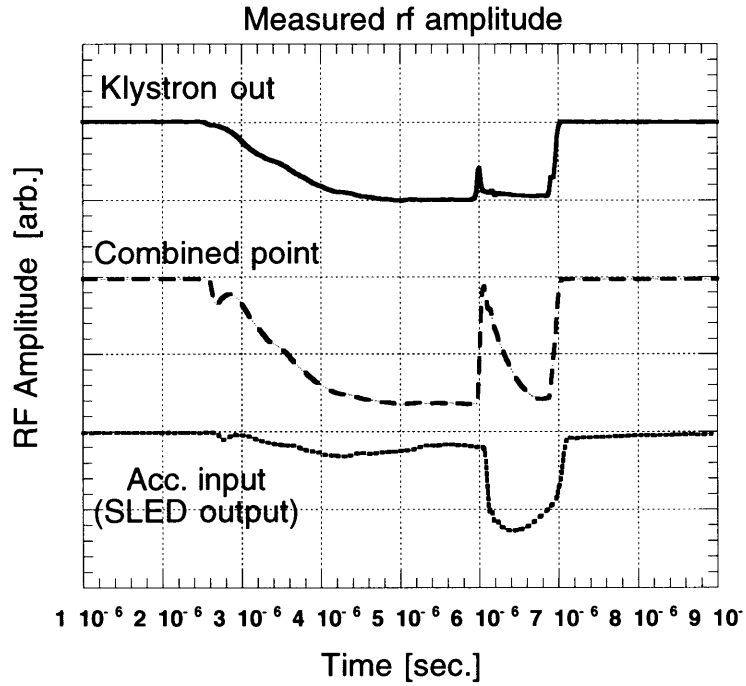

Figure 4.15: The measured rf amplitude at the output of klystron, the combined point and the input of accelerating structure (SLED output) with the phase rotation speed at 90 degrees/800 ns.

vector to two components (X_i,Y_i). X_i is the real and Y_i is imaginary part of the rf vector. By measuring this two components and using Eq B.6, we can get the phase value of the rf signal. Figure 4.16 shows the two components of the rf vector for the klystron output and the combined point in which phase rotation speed was 90 degrees/400 ns. Figure 4.17 shows the measured rf phase of klystron output and combined point after rf phase reverse. The rf phase of klystron output was rotated by changing drive rf phase as shown in upper figure of Figure 4.17. On the other hand, as shown in Figure 4.17 the rf phase at combined point was kept in some range while the phase of klystron drive rotates.

4.2.3 Measurement system of the beam energy

Figure 4.18 shows the layout of the beam line to measure the energy variation along the bunch train.

For energy measurement, the horizontal chicane was installed downstream of the four regular accelerating structures which were filled amplitude modulated rf power. This chicane contains a strip-line-type beam position monitor (BPM) and a beam profile monitor which were mounted at the center of the chicane to measure the beam energy and observe the beam profile. At this BPM, the horizontal dispersion function η_x was 50 mm. The multi-bunch beam signal from the BPM was measured by using a digital oscilloscope of real-time 5.0 GHz sample and a personal computer as shown in Figure 4.20. A pulse height of each bunch signal was determined by a parabolic curve fitting to the sampled data. In this measurement, the position resolution was about 130 μm which was derived from three BPMs correlation and this position resolution corresponds to 0.26 % energy resolution. The position resolution was mainly limited by a systematic error of the fitting, so it may be improved using other functions for the fit. On the other hand, the only horizontal orbit of all bunches in the same pulse was measured using 7 BPMs in the linac, this measurement was free from the pulse-to-pulse energy jitter.

4.2.4 Preliminary result of beam test

In this experiment, the multi-bunch of 19 bunches/pulse accelerated with intensity of 0.82×10^{10} electrons/bunch at pre-injector exit. This beam intensity was derived from the measured beam loading voltage at analyzer magnets downstream. At the 80 MeV point, the energy of multi-bunch beam was compensated using the simple ΔT compensation technique (only early injection) to make the flat energy distribution as an input of $\Delta\phi$-A compensation section.

We observed the difference of compensating voltage along the multi-bunch beam by changing the phase rotating speed and the relative timing of rf pulse to the beam in the two klystrons. Figure 4.22 shows rf waveforms at the input

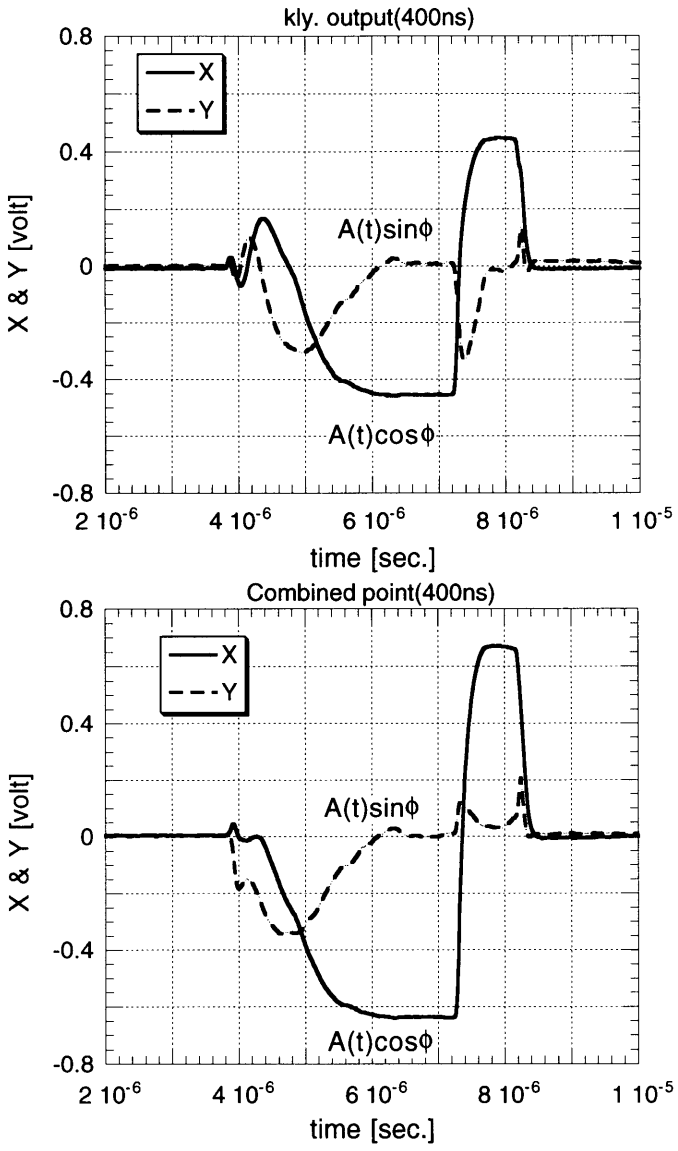

Figure 4.16: The measured X and Y component of rf vector using the phase detector with the phase rotation speed at 90 degrees/400 ns. The upper figure is the case of fast phase rotation and the lower figure is the case of slow rotation of drive rf phase.

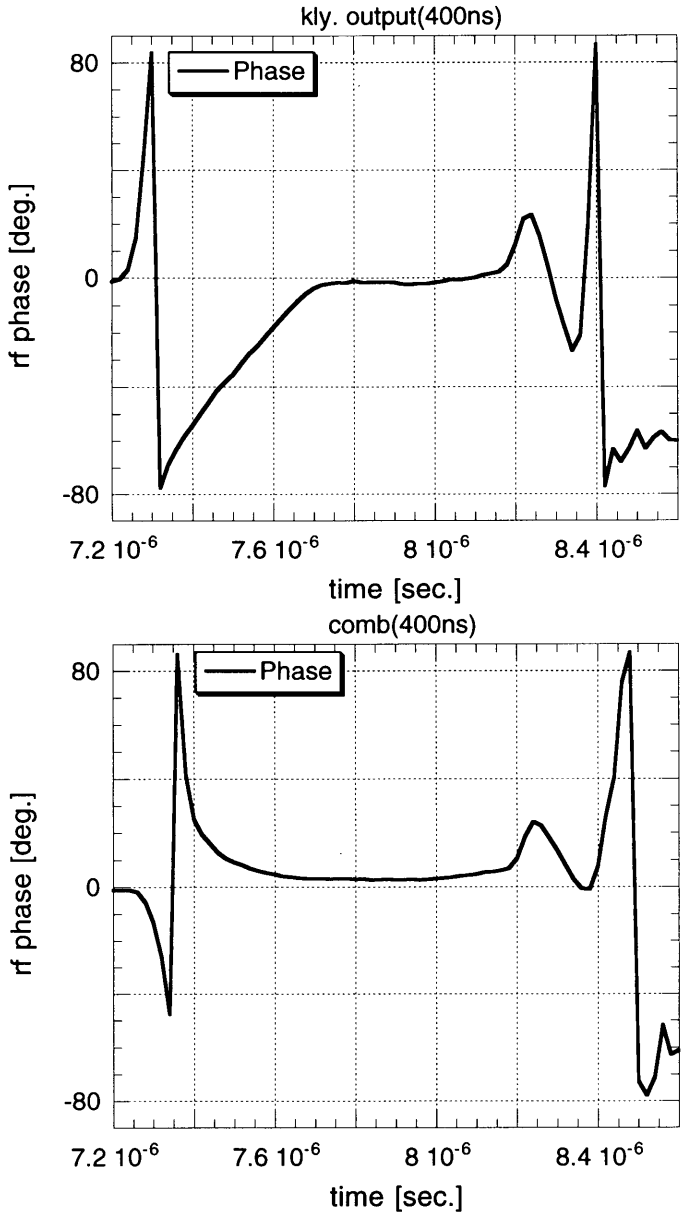

Figure 4.17: The measured rf phase of the klystron output and the combined point during phase rotation of klystron drive. The drive rf phase of klystron was changed with the rotation speed at 90 degrees/400 ns after 7.25 *mus* in the figure.

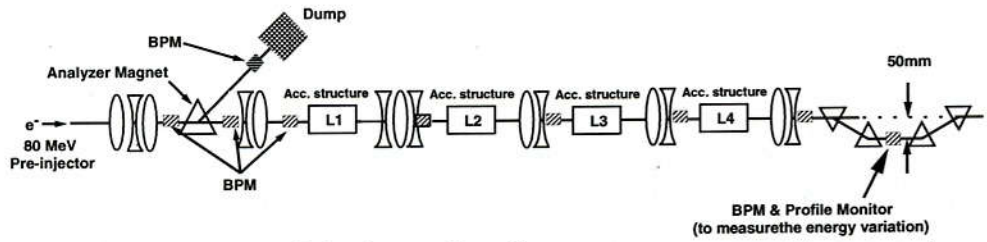

Figure 4.18: Layout of the beam line for energy compensation experiment

Figure 4.19: Photograph of the chicane to measure the multi-bunch beam energy at the middle of linac. The chicane was constructed by four dipole magnets and it contains a beam position monitor and beam profile monitor.

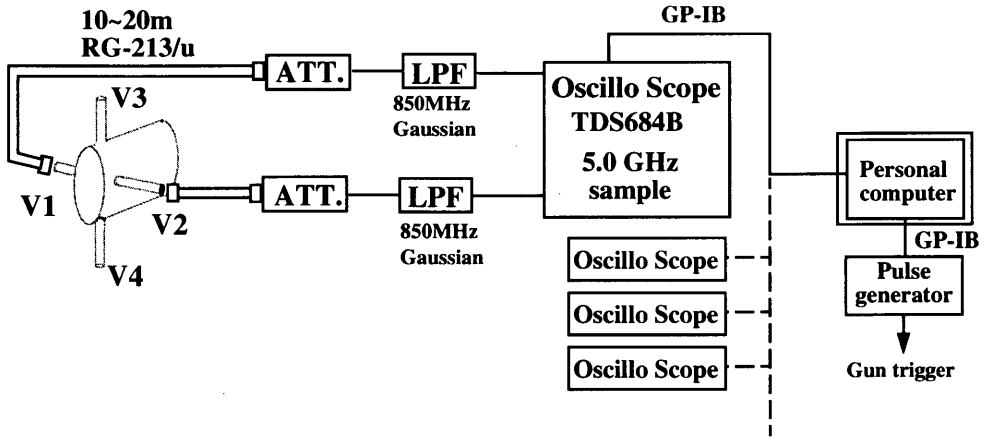

Figure 4.20: BPM read system.

of accelerator and the combined point in the two cases of different rotating speed of drive rf phase. The calculation result of unloaded energy gain slope for the previous two different phase speed is shown in Figure 4.23. In this calculation, klystron output power is assumed to be 20 MW which is the same value with the real beam test setup and the parameters of SLED cavities and structure are also the same. The two slopes of the unloaded energy gain curve are different due to the different waveform of SLED output is fed to the accelerating structure. In the slow rotation case in which the phase speed is 90 deg./800 ns, the compensating voltage is larger than the other case (see in Figure 4.23). Figure 4.24 shows energy distribution of multi-bunch beam at the chicane in the two different rotating speed of drive phase and the two different beam injection timing to rf pulse which are shown as timing (A) and (B) in Figure 4.23. Assuming that the beam loss at $\Delta\phi$-A compensation region was 10 % at the entrance of the first structure, the calculated beam loading voltage was about 2.7 MV/structure. Then the calculated energy spread with 90 deg./400 ns rotating speed are about 4.0 % at timing (A) and 1.8 % at timing (B), while in the another case with 90 deg./800 ns rotating speed they are about 2.8 % and 0.5 % at the each timing. From the Figure 4.24, the measured energy spread were 4.5 % (with timing A) and 1.5 % (with timing B) for 90 deg./400 ns, 2.6 % (with timing A) and 0.5 % (with timing B) for 90 deg./800 ns speed. The calculated values and the measured energy spread were consistent, so the amplitude modulation of the input rf acted to the multi-bunch beam so as to compensate the beam loading. However, the measured energy distribution inside the multi-bunch beam had a fluctuation from monotonous change. This fluctuation correlated to the intensity of each bunch. If we can measure the intensity variation along the bunch train and monitor the rf power correctly, the energy spread of multi-

bunch beam will be minimized by setting the rotating speed of rf phase and injection timing as calculated.

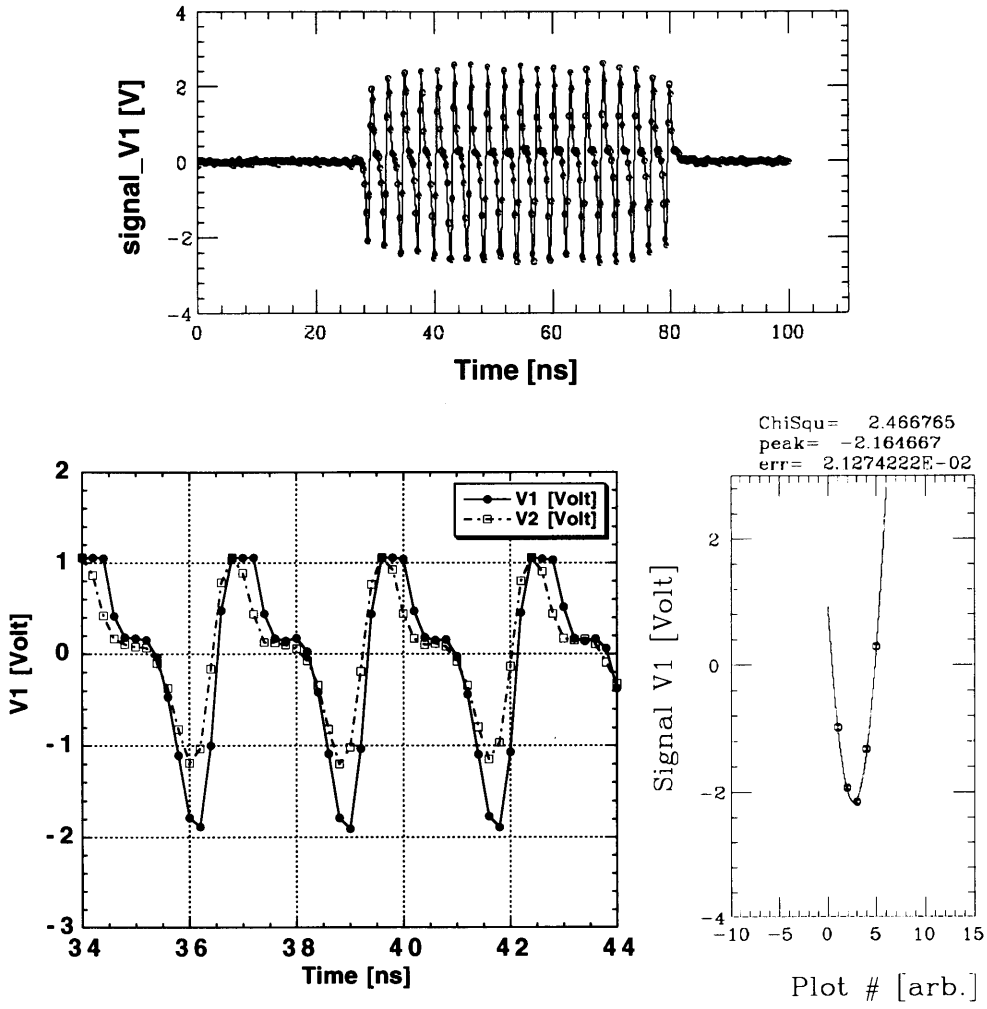

Figure 4.21: Measured beam signal from the horizontal electloads of strip-line BPM and the example of fitting to sample data.

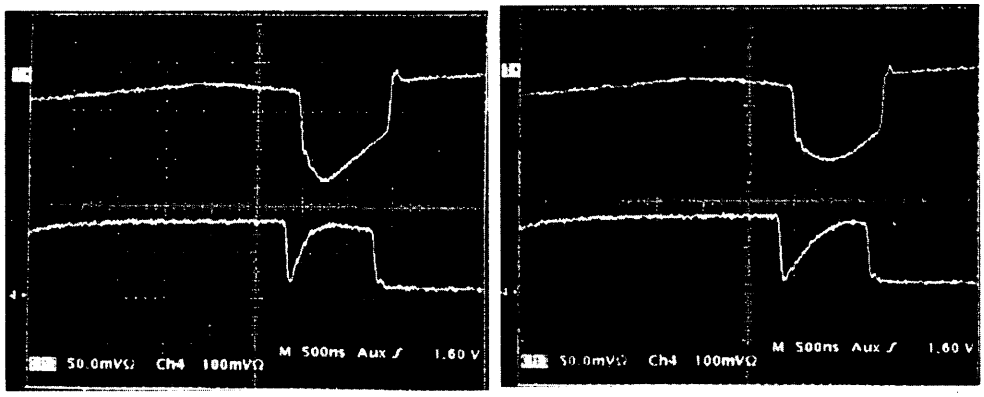

Figure 4.22: Rf waveform at the structure input (up) and the combined point (down) in different phase rotating speed. (right:90 deg./400 ns, left:90 deg./800 ns)

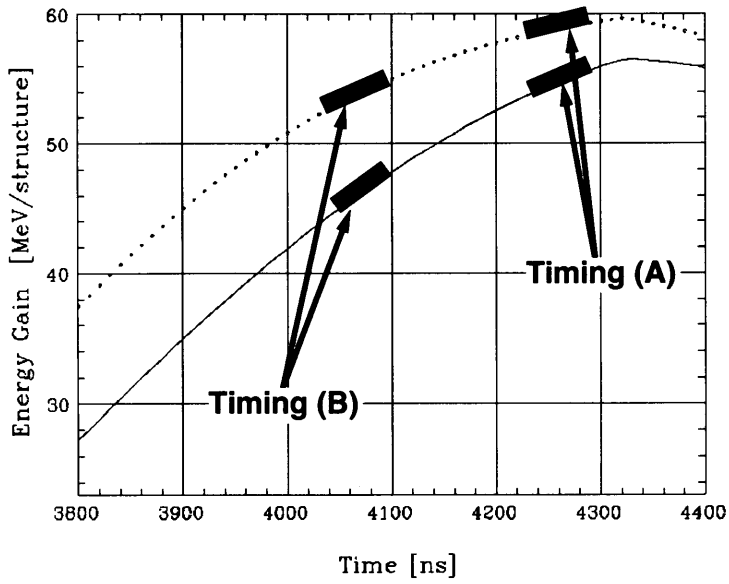

Figure 4.23: The dashed line and solid line shows calculation result of unloaded energy gain in the two different phase rotating speed. In the case of dashed line, the phase rotating speed is 90 deg./400 ns, the case of solid line is 90 deg./400 ns.

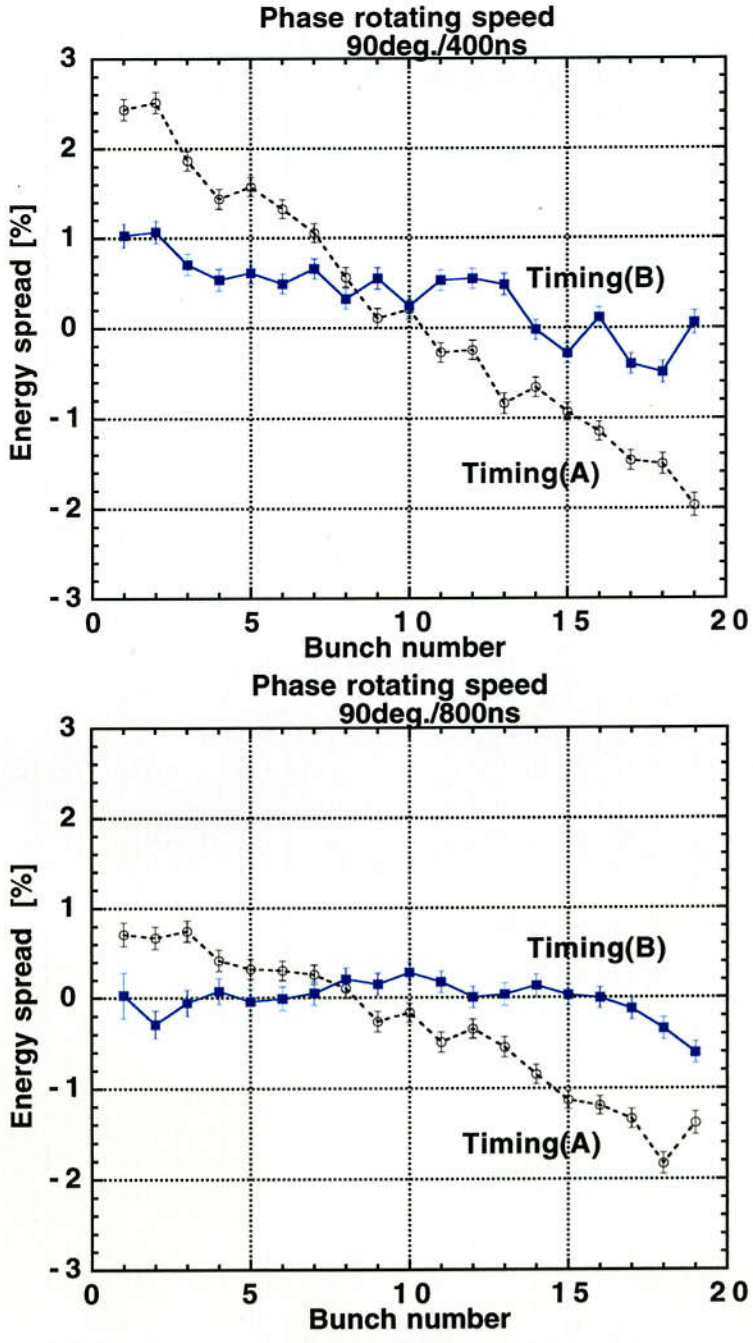

Figure 4.24: Measured multi-bunch energy spread with different speed of phase rotation (Upper:90deg/400ns Lower: 90deg./800ns). In the both figures, the circles and the black squares show the multi-bunch energy distribution with timing(A) and timing(B).

5 Conclusion

We compared with the two different types of multi-bunch energy compensation methods in the linacs using tracking simulation, one is local compensation method and another one is unlocal energy compensation method. From simulation results, the local energy compensation method is able to suppress the emittance growth due to the chromatic effect than the unlocal energy compensation method. In the case of ΔF energy compensation the oscillation of transverse motion increase by the energy spread between head and tail in a single bunch in the accelerating structure, because each bunch is accelerated on the negative and positive sinusoidal slopes of rf-wave in the $\pm\Delta F$ structures. The results of this simulation would gave the good information for the choice of energy compensation method in the S-band linac of future linear colliders.

In ATF linac, we performed the beam test of the ΔF and $\Delta\phi$-A energy compensation methods. The beam test of the ECS was performed using 2856$\pm$4.327 MHz structures in the ATF linac. When the measured energy difference was about 1.5 %, the ECS could compress it to 0.5 % with 3.2×10^{10} total intensity. The single-bunch energy spread was less than about 0.5 % at the case of total charge/pulse = 3.2×10^{10}. Clear compensation of single bunch energy spread by the effect of a negative and positive slope in the compensating section was not observed in these low compensating voltage. However the principle of ΔF ECS for multi-bunch beam was verified.

The beam test of $\Delta\phi$-A energy compensation was also performed by using two klystron combination. Phase modulation of two klystrons was used to modulate an rf amplitude of SLED-I input at constant phase. Energy gain of each bunch along a bunch train was changed by modulating the amplitude of structure input rf, as a result the beam loading of multi-bunch beam was compensated as expected.

From the result of the simulation, we understood that the local energy compensation method has good advantage for the emittance growth. So as next step, it is necessary to develop the useful control systems of $\Delta\phi$-A energy compensation method for future linear colliders.

6 Acknowledgments

I would like to express the my greatest thanks to Professor K. Oide who gave me the opportunity and the supports to write this paper. This work has been carried out at KEK/ATF, and this work could not have been carried out without the support and many comments and discussion with Professors S. Takeda, J. Urakawa, H. Hayano, K. Kubo, N.Terunuma, S. Kuroda, N. Toge, T. Naito, S. Araki, M. Akemoto and T. Korhonen. Their help is greatly appreciated and I learned the great deal of my basic accelerator physics. Especially I am grateful for critical reading of the manuscript by H. Hayano and K. Kubo. I would like to acknowledge the continuous encouragement of Professors Y. Kimura, M. Kihara, Y. Yamazaki and S. Kurokawa. I would like to express thanks to Professor M. Yoshioka who gave me the opportunity to study the accelerator science in KEK. I would like to thank Professor T. Shintake who gave many useful comments for the phase to amplitude modulation method and the supports to write this paper. I would like to acknowledge Professor H. Matsumoto who gave the many expert knowledges and the continuous encouragement. I would like to acknowledge all the member of the ATF group, the graduate students and the member of E-CUBE Corp. and Kantou-jouhou Corp. for their useful discussion, cooperation and support. I would like to acknowledge all the member of KEK/SLAC linear collider group for discussion and grateful support and especially I am grateful for the useful comments by K. Yokoya, T. Higo and M. Yamamoto of IHI Corp. I would like to acknowledge the continuous encouragement of Professors S. Nakamura and Y. Maeda, they also gave me the opportunity to study the accelerator science in KEK. I also appreciate to Drs. T.Shidara and H.Honma of photon factory division in KEK for the reason that they have readily lent us the pulse modulators for the ECS. I also appreciate to Drs. K. Egawa and M. Masuzawa of accelerator laboratory in KEK for the reason that they have readily lent us the dipole magnets.

In conclusion, I express my hearty thanks to my parents and brothers.

Appendix

A Wakefields of S-band structure

A.1 Parameter of the accelerating structure

The main parameters of the conventional SLAC type S-band accelerating structure are listed in Table A.1. Figure A.1 shows the size of the half iris aperture and the cell radius.

Table A.1: Main parameters of the S-band accelerating structures.

Operating frequency	2856 MHz
Phase shift/cell	$2\pi/3$
Electric-field distribution	Constant gradient
Structure length	3 m
Number of cell	84 cells + 2 couplers
Quality factor	13,000
Shunt impedance	60 MΩ
Attenuation parameter	0.57
Group velocity	0.0204—0.0065 C
Filling time	0.83 μs

A.2 Wakefield calculation

A.2.1 Short range Wake-Field

The short-range transverse and longitudinal wakefunctions, $W_L(s)$ and $W_T(s)$ were calculated using following formulas which was derived by K. Yokoya [50] [8].

For the longitudinal wake function,

$$W_L(s) = \frac{cZ_0}{\pi a^2}(1 + W_{L1}\sqrt{\zeta} + W_{L2}\zeta + W_{L3}\zeta\sqrt{\zeta}), \tag{A.1}$$

and for transverse wake function,

$$W_T(s) = \frac{cZ_0}{\pi a^4}(2 + W_{T1}\sqrt{\zeta} + W_{T2}\zeta + W_{T3}\zeta\sqrt{\zeta}), \tag{A.2}$$

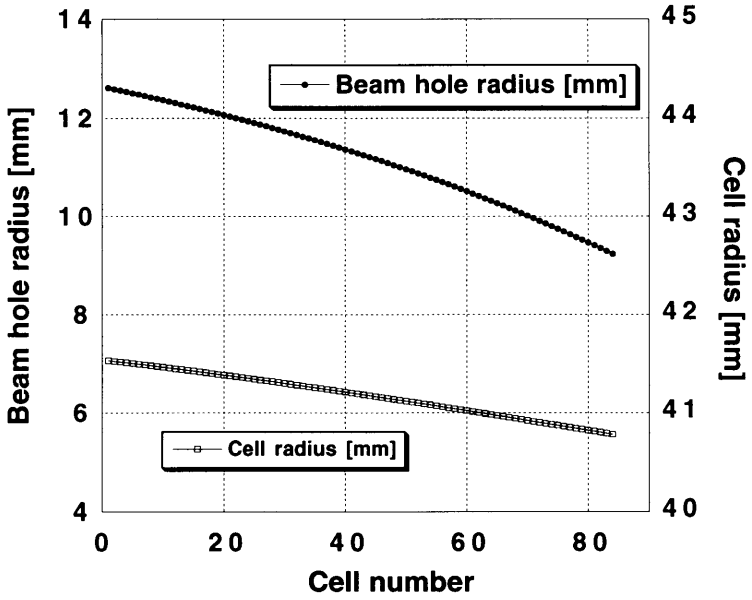

Figure A.1: The half iris aperture and the cell radius as function of the cell number

where

$$\begin{aligned} \zeta &= \frac{Ls}{a^2}, \\ L &= \text{cavity cell period}, \\ \lambda &= \text{wave length}, \\ a &= \text{iris aperture}, \\ Z_0 &= \text{vacuum impedance}. \end{aligned}$$

The coefficients are given by

$$\begin{aligned} W_{L1} &= -1.614r^{0.122}, \\ W_{L2} &= 1.012r^{0.169}, \\ W_{L3} &= -0.231r^{0.111}, \\ W_{T1} &= -2.781r^{0.217}, \\ W_{T2} &= 1.637r^{0.511}, \\ W_{T3} &= -0.364r^{0.793}, \end{aligned}$$

where

$$r = \frac{a/\lambda}{0.15}.$$

Eq. A.1 and Eq. A.2 were computed in the following parameter range about the iris aperture and the disk thickness.

$$0.10 = \frac{a}{\lambda} = 0.20,$$
$$0.11 \leq \frac{L-g}{L} \leq 0.25.$$

The formulas are valid in the range $0 \leq s \leq 0.2L$. In our simulation, the parameters a/λ and (L-g)/L are used 0.1035 and 0.14285, respectively. Figure A.2 shows the transverse and Figure A.3 shows the longitudinal wake function for the S-band structure.

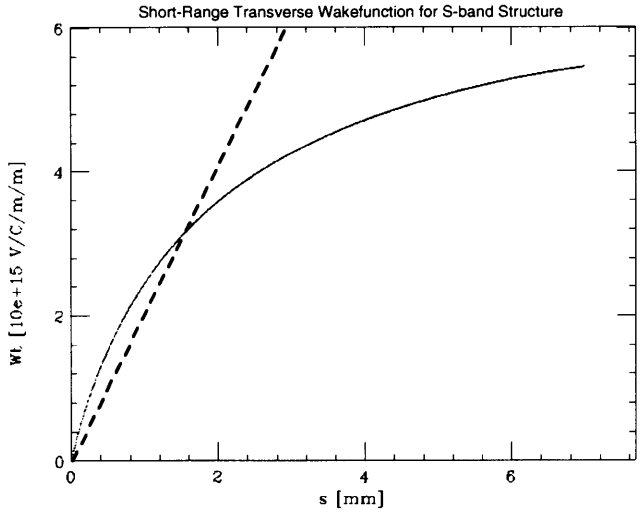

Figure A.2: Short range Transverse wake function. The dashed line shows the linear approximation used in our tracking simulation.

A.2.2 Long range Wake-Field

The long-range transverse wakefield was calculated by using the "open mode expansion" for S-band simple disk loaded structure [51]. The frequencies, kick factors and field distribution of all the modes in the passband from the lowest to the 8'th one were derived. This result is shown in Fig A.4.

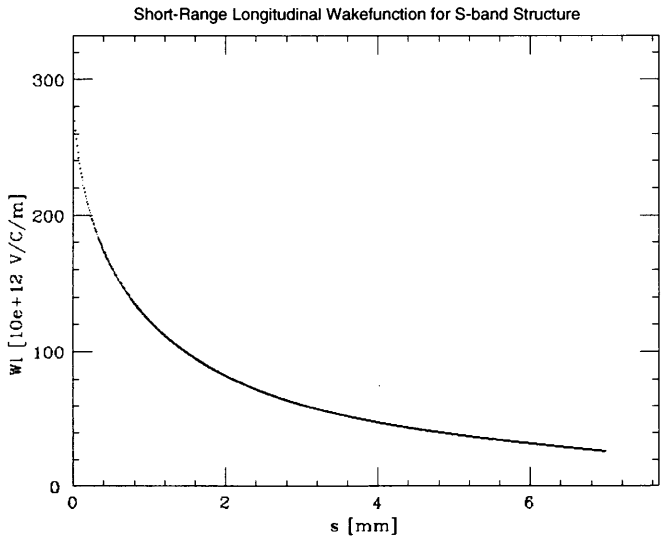

Figure A.3: Short range longitudinal wake function.

The wakefield can be calculated from this result as the sum of all the modes as

$$W_{\tau(t)} = \sum_{m}^{all} 2k_T^m sin(\omega_m t) \tag{A.3}$$

where k_T^m and ω_m are the kick factor and frequency of the mode m. The transverse wake field of conventional S-band structure are plotted in Fig A.5. In this case, we assumed that the Q-values for all of the modes are infinite. The Q-values are almost the same for all the modes and we can estimate the reduction at the end of train from multiplying each mode by $exp(-(\omega_m s/2Q_c)$.

Effects of the long range longitudinal wake are taken into account as the different energy gain of different bunches in a train. The amplitude of the accelerating voltage at nth bunch injected at t is

$$\Delta E_{total} = \int_0^L E(s,t)ds + \Delta V_{bl,nth} \tag{A.4}$$

where $E(s,t)$ and $\Delta V_{bl,nth}$ are given as Eq 1.10 and Eq 1.24.

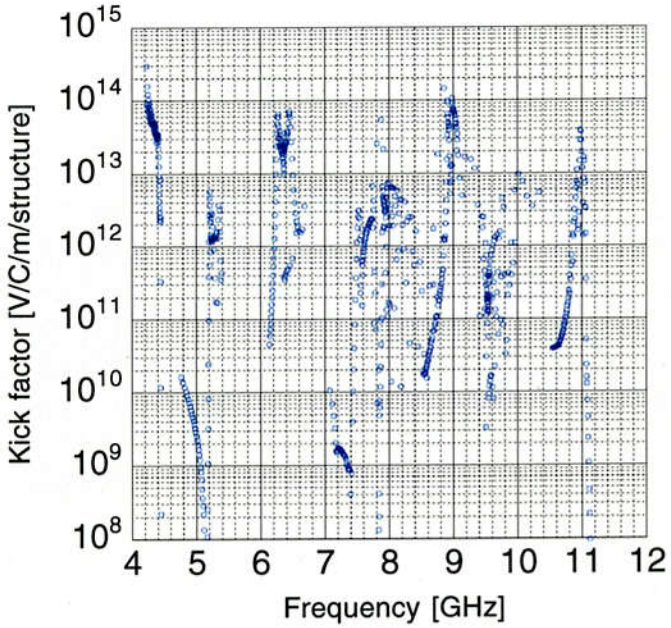

Figure A.4: Calculated kick factors of the modes in the 84-cell simple disk loaded S-band structure. Calculations have been done by open mode expansion method.

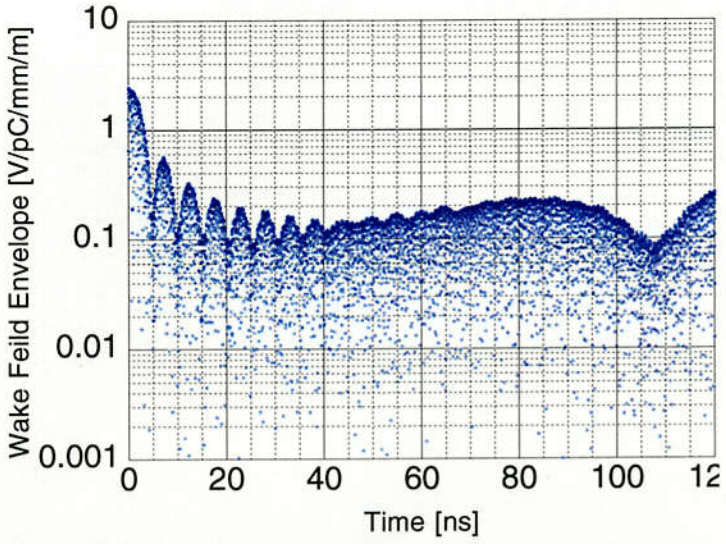

Figure A.5: Wake field for the simple disk-loaded S-band structure

B RF measurement

B.1 RF detector

We used the rf detector (HP8473B 0.01-18 GHz) to measure the rf power at the some point. The rf detector was calibrated using the synthesized signal generator (HP8663A), a frequency doubler, the CW rf power meter (HP438A/HP8418A), a digital multi-meter and variable attenuator (shown in Figure B.6). Figure B.7 shows the calibration results, in which the detected

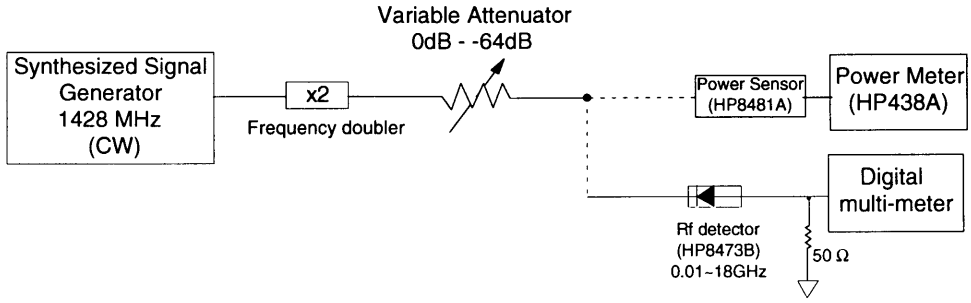

Figure B.6: Setup of rf detector calibration measurement.

voltage using the rf detector was approximately linear response as a function of input rf amplitude. We measured the rf power within this linear region.

B.2 RF phase detector

B.2.1 Principle of rf phase detector

We used the rf phase detector (which was made by NEC corporation) to measure the rf phase of klystron output and the combined rf of two klystrons output [52][53]. In this phase detector, an rf vector $\boldsymbol{A}$ is decomposed to two components (X_i, Y_i). X_i is the real part and Y_i is the imaginary part of $\boldsymbol{A}$. On a complex plane, $\boldsymbol{A}$ is represented by the arrow $\boldsymbol{OA}$ as shown in Figure B.8. The magnitude and the phase angle of $\boldsymbol{A}$ are written by

$$|\boldsymbol{A}| = \sqrt{X_i^2 + Y_i^2} \tag{B.5}$$

and

$$\phi = \tan^{-1}(\frac{Y_i}{X_i}). \tag{B.6}$$

We can get the rf phase by measuring the voltage signals which proportional to X_i and Y_i. The circuit block diagram of the phase detector is shown in Figure B.9

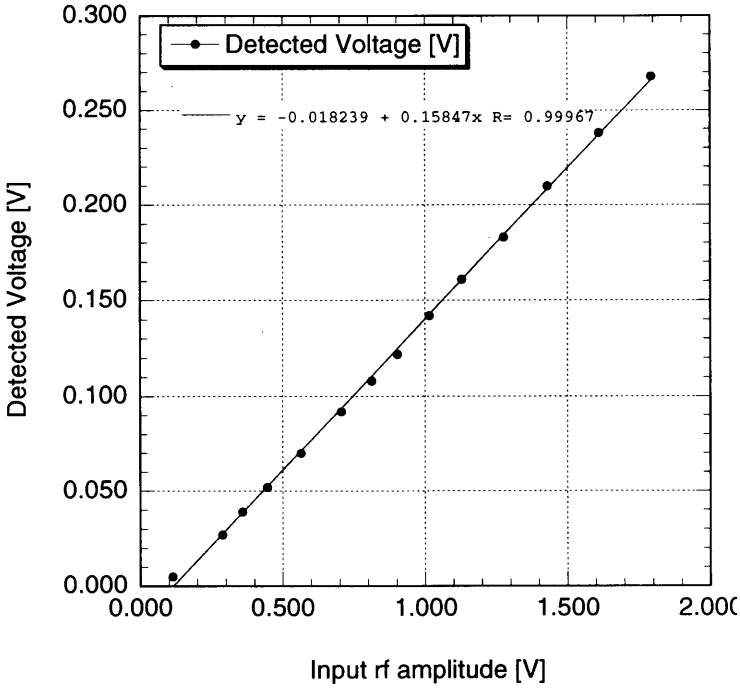

Figure B.7: The result of calibration measurement of rf detector (HP8473B). Horizontal axis is the input CW rf amplitude, vertical axis is detected voltage through the rf detector.

In Figure B.9, E1~E4 are written by

$$\begin{aligned} E1 &= Ae^{j(\omega t+\frac{\pi}{2})} + Be^{j(\omega t+\phi+\pi)} \\ E2 &= Ae^{j(\omega t+\pi)} + Be^{j(\omega t+\phi+\frac{\pi}{2})} \\ E3 &= Ae^{j(\omega t+\frac{\pi}{2})} + Be^{j(\omega t+\phi+\frac{\pi}{2})} \\ E4 &= Ae^{j(\omega t+\pi)} + Be^{j(\omega t+\frac{\pi}{2})}, \end{aligned} \tag{B.7}$$

and the output voltage signal S1 and S2 are

$$\begin{aligned} S1 &= g1(E2-E1) \approx -4g_1kAB\sin\phi \propto X_i \\ S2 &= g2(E3-E4) \approx 4g_2kAB\cos\phi \propto Y_i \end{aligned} \tag{B.8}$$

where g_1, g_2, k, A and B are the gain of differential amplifiers, the conversion coefficient of diode, the amplitude of reference signal and measured rf signal, respectively. Here we assumed that the 4 hybrid circuits ideally work as 90 degrees hybrid junction, the 4 diodes have the same conversion coefficient. In general, the output voltage of diode V_{out} is written as

$$V_{out} = k|E_{in}|^n \tag{B.9}$$

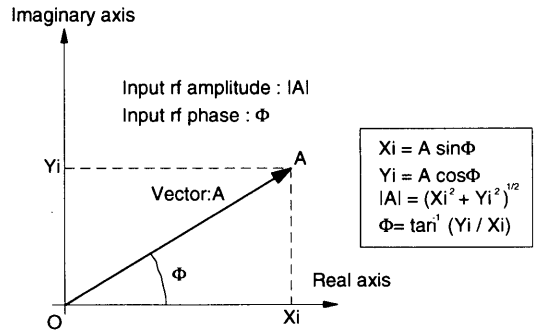

Figure B.8: Vector decomposition for rf signal

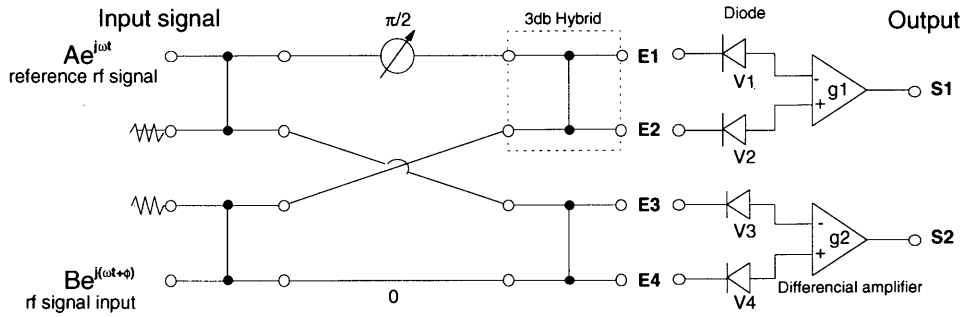

Figure B.9: The circuit block diagram is phase detector

where k and n are conversion coefficient and detection curve of diode, and E_{in} is the amplitude of input signal. The n=2 was assumed in Eq B.9. The phase value of an input rf signal is calculated by a Eq. B.6 and Eq. B.8.

B.2.2 Calibration of the phase detector

Figure B.10 shows the setup of phase detector calibration measurement. Input power level of the reference rf signal is +7 dBm and one of the test signals are changed to -10 dBm,-20 dBm and -30 dBm using variable attenuator. Figure B.11 shows the measurement result which is polar plot of the phase detector output voltages in a complex plane. The X and Y are correspond to $r \sin \phi$ and $r \cos \phi$ where r and ϕ are the magnitude and phase angle.

Figure B.12 shows the detected phase error as a function of setting phase which is set by the mechanical phase shifter. This mechanical phase shifter was calibrated using the network analyzer (HP 8753B) at S_{12} mode.

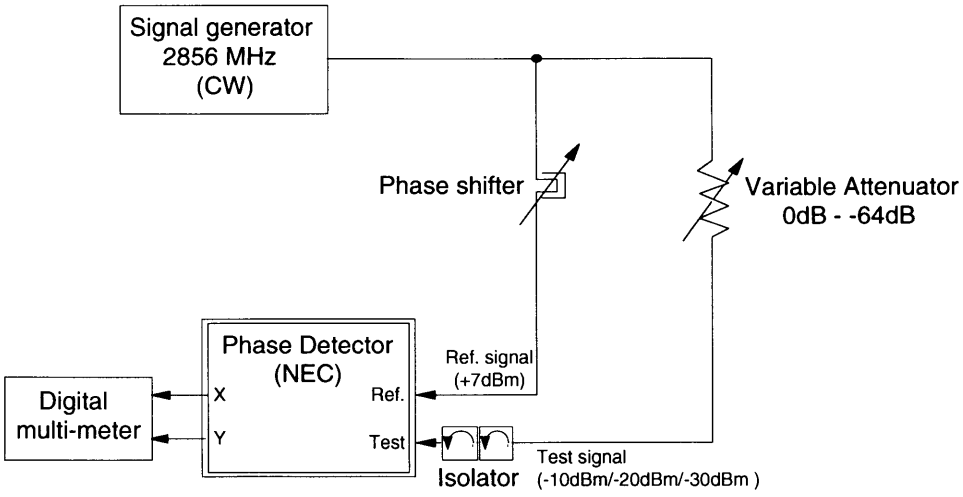

Figure B.10: Setup of phase detector calibration measurement.

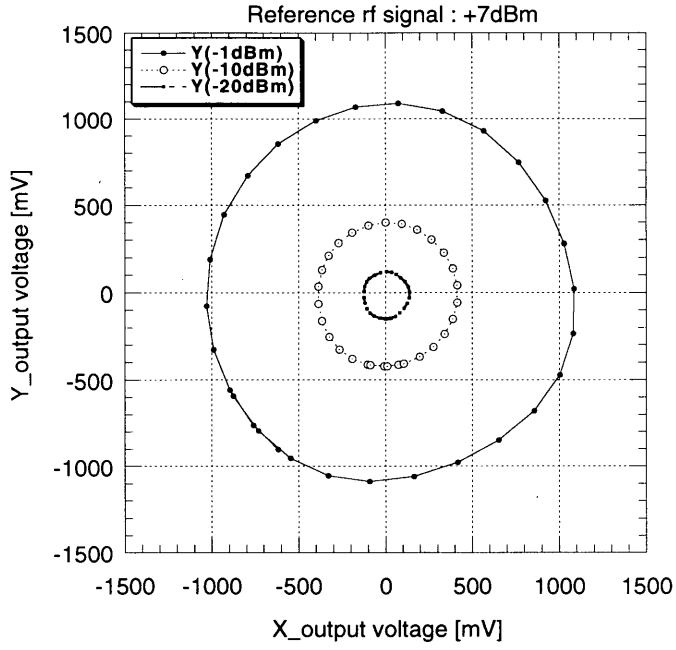

Figure B.11: Polar plot of the phase detector output voltages on a complex plane. Input power level of the reference rf signal is +7 dBm and one of the test signals are -10 dBm, -20 dBm and -30 dBm.

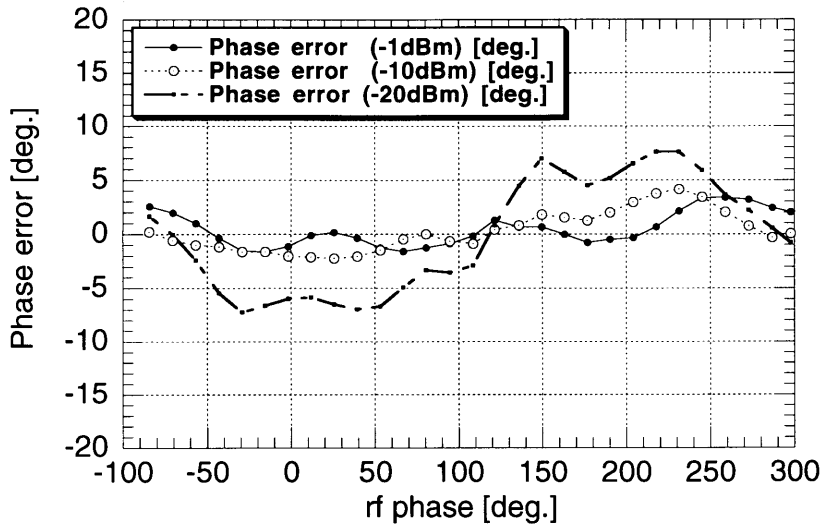

Figure B.12: The measured phase error of the phase detector.

C Accelerating Text Facility (ATF)

Accelerator Test Facility (ATF) was constructed in the TRISTAN Assembly Hall for linear collider R&D [54]. ATF consists of 1.54 GeV S-band linac, beam transport line, damping ring and extraction line (Figure C.13). As the future plan, a bunch compressor and rf unit of main-linac would be installed. The 1.54 GeV S-band linac is injector of the the damping ring supplies a multi-bunch beam which is 20 bunches with 2.8 ns bunch spacing.

The main purpose of ATF is to develop an the extremely low emittance beam (1×10^{-11} m for vertical). This is an essential requirement for getting the high collision luminosity in linear colliders. ATF linac is not only a injector linac of the damping ring but also test accelerator for the key components to realize a linear collider such as multi-bunch generation, high gradient acceleration [55], energy compensation for beam loading and beam instrumentation development.

The commissioning of the linac has started on November 1995 and a beam acceleration of a single bunch and multi-bunch beam were succeeded at 1.3 GeV [56]. The experiments of multi-bunch energy compensation for the transient beam loading using ΔF method were performed [57]. After five months of linac operation, the components of the damping ring were installed and aligned at the inside of housing tunnel. The beam commissioning of the damping ring started the end of January 1997. At first, the damping ring was operated with 0.96 GeV energy and single bunch beam with 6.0×10^9 electrons was stored in the run of the first three months. After short shut down, the beam energy was raised to 1.3 GeV with single bunch beam [58].

C.1 ATF S-band Linac

The S-band injector linac is designed to accelerate multi-bunch beam for injection to the damping ring. This injector linac consists of an 80 MeV pre-injector linac, 8 units of regular accelerator sections and two units of energy compensation accelerating structures.

C.1.1 Multi-bunch beam generation

The thermionic gun for multi-bunch generation has been developed in ATF. The thermionic gun uses a triode cathode and operates up to 240 kV of pulsed high voltage. The development of a grid pulser system is very important issue of the multi-bunch generation. High intensity single bunch has been already generated using avalanche pursers [59][60]. This grid pulse for multi-bunch beam consists of fast ECL circuit, a pair of signal transmitter and receiver system and an RF power amplifier.

A 357 MHz RF signal for grid pulser system is synchronized with the

accelerating frequency and it is used as a clock signal to the ECL circuit. The system trigger hits other components of the linac through synchronizing and delay circuit [43]. The required number of bunches are formed counting and gating the clock in the circuit.

RF power amplifier has been developed for the grid pulser by NEC corporation. Since this amplifier is used on high voltage potential, the size, plug power and so on are limited. Therefore the peak power and band width are sacrificed. The waveform of amplifier output has the slow rise and fall time of the envelope which is caused by the narrow band width.

In the beam test of $\Delta\phi$-A ECS, to get the intensity uniform of multi-bunch beam, we modify the grid pulser system. we tried to get uniform multi-bunch beam by combining output waveform of RF amplifier and a rectangular pulse of 400 V pulse generator output as shown in Figure C.15.Emission current was measured using current transformer (CT) and a wall current monitor(WC) at just down stream of the thermionic gun and down stream of first accelerating structure as shown in Figure C.16.

C.1.2 80 MeV Preinjector of Linac

Figure C.14 shows the layout of ATF 80 MeV preinjector which consists of the thermionic gun, two 357 MHz sub-harmonic bunchers (SHBs), S-band buncher cavities and a 3m-long accelerating structure. The role of preinjector is to generate the 20 bunches of 2×10^{10} electrons/bunch with 2.8 ns bunch spacing and to inject the multi-bunch to regular sections of S-band injector linac. The generation of multi-bunch beam from ordinary thermionic gun is done by applying rf signal of 357 MHz to the grid [61]. The emitted bunches from the gun has about 1 ns (FWHM) bunch length with 240 kV energy. The two SHB cavities and S-band buncher cavities compress the bunch and the bunches are accelerated to 80 MeV by a 3m-long accelerating structure. In preinjector section, one klystron is used without SLED system and the rf pulse waveform from the klystron for the S-band accelerating structure is rectangular with a width of 1.0 μs.

C.1.3 Accelerator Section of the ATF Injector Linac

The length of the accelerator section of S-band ATF injector is about 80 m including accelerating structures, quadrupole and dipole magnets and beam monitors. The high gradient is used for the beam acceleration. The regular unit is composed by 80 MW klystron (TOSHIBA E3712), two-iris SLED [41], rf dummy loads and two 3m-long high gradient accelerating structures. Using SLED pulse compression system, the extracted rf peak power from the SLED cavities is increased to 400 MW (200 MW peak power rf into 3m-long structure) and 240 MeV energy gain in a regular rf unit. The linac components are aligned on a precise L-type support table. The stages of linac

for the accelerating structures and magnets have an active mover mechanism and wire position sensors which were used to monitor the stage position and to align [62].

C.1.4 Beam monitors

In order to measure the multi-bunch beam orbit, the beam position monitor (BPM) system were installed in the linac. The pickup chambers are button-type BPM for the pre-injector and strip-line type BPM for the linac and beam transport line. All BPMs were measured the relation between an electrical and a mechanical center, and their position detection sensitivities by using fast pulse transmission method with coaxial structure. The results of measurement show that the BPMs have constant sensitivity coefficient within ± 1 mm from the mechanical center. The uniformity of the BPMs have $\pm 10 \mu$m at that range [63].

The transverse beam profile was measured by the phosphor-screen profile monitors (PRMs), wire scanner and optical-transition radiation monitors (OTRMs). The beam-profile measurement of each bunch was performed by using a fast gate camera and OTR monitors [46]. Since transition radiation is generated by each electron in a bunch, it carries information concerning the bunch structure. The OTR monitor was used to measure the bunch length in bunch by bunch using streak camera [64].

The beam current was measured by an amorphous core current transformer (CT) and wall current monitor (WC). This WC monitor has the capability of fast current measurement.

C.2 ATF Damping Ring

The ATF Damping Ring has been designed to operate at 1.54 GeV and can store up to five multi-bunch trains. The damping ring has a race-track shape, consisting of two arc sections. The ring circumference is 138.6 m. The target equilibrium emittance are $\gamma\epsilon_x = 5.0\times10^{-6}$ m and $\gamma\epsilon_y = 3.0\times10^{-8}$ m. For this purpose, a special design of a strong-focusing FOBO lattice is implemented using the combined function bending magnets in the arc section. The two straight sections are dispersion free sections, and they accommodate injection and extraction septum magnets, RF cavities, and damping wiggler which reduce the radiation damping time by a factor of 1/2 [65].

Total 96 sets of BPMs were installed in the damping ring for measuring the beam orbit in an arbitrary turn. In order to measure the beam profile in the damping ring, a synchrotron radiation monitor has been installed near the exit point of the arc section. Now a laser wire system is under development to measure the extreme small beam size.

The lattice diagnostics have been performed in the ATF damping ring.

Error of quadrupole strengths of the quadrupole magnets and the combined bending magnets have been estimated using beams, by steering beam and measuring the orbit in down stream. The measured response coefficients are fit by errors of strength of quads, BPMs and steerings [66].

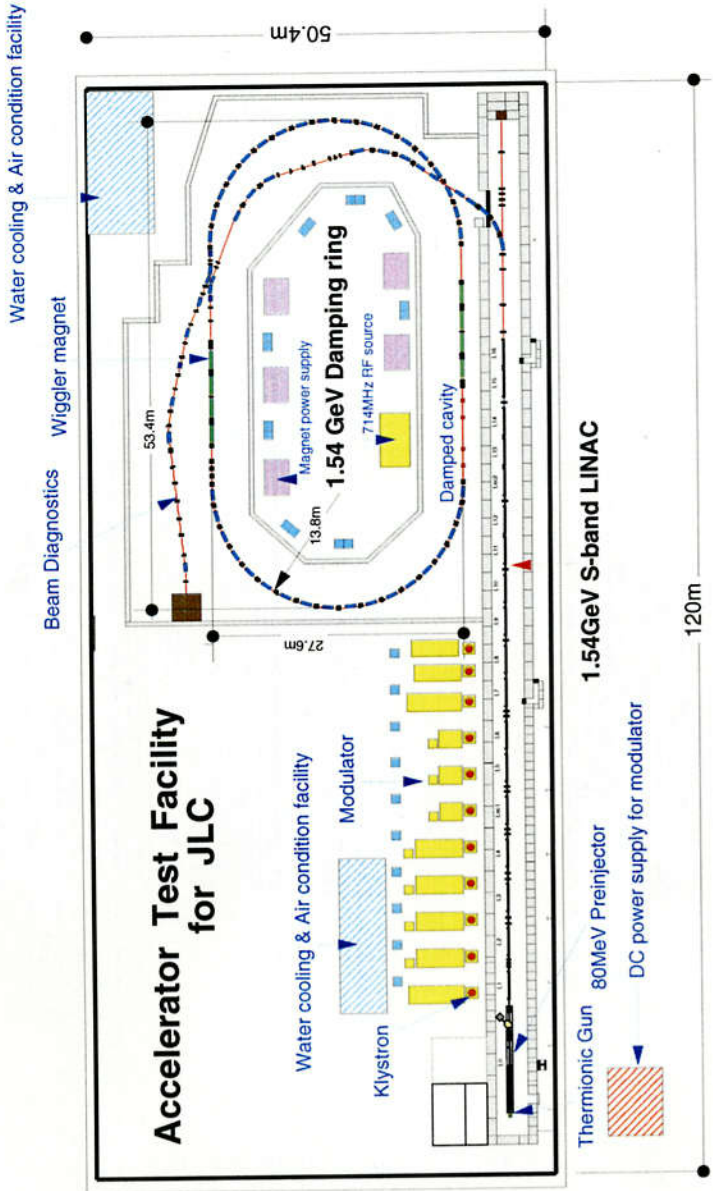

Figure C.13: ATF Overview.

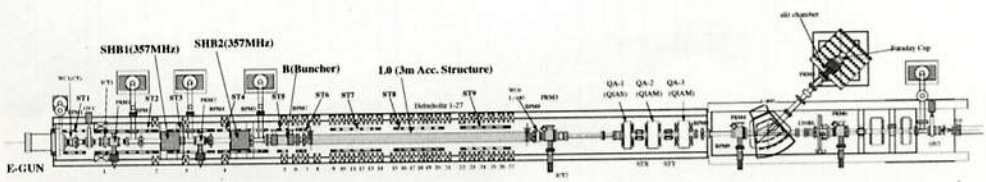

Figure C.14: Layout of ATF 80 MeV pre-injector.

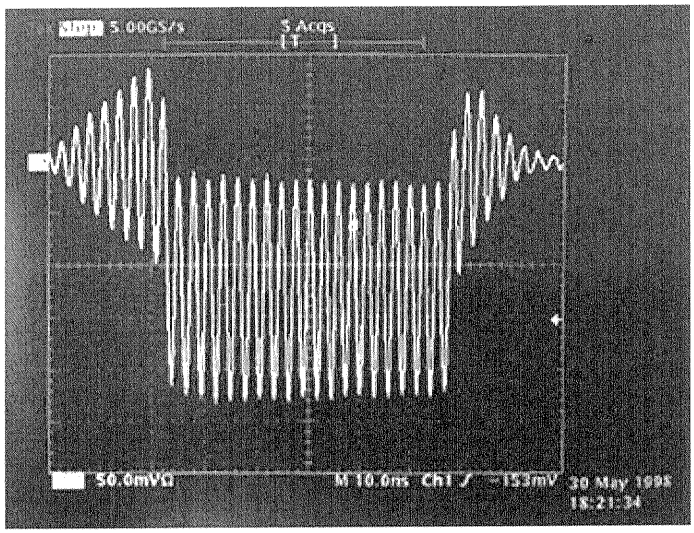

Figure C.15: Enhanced burst RF waveform.

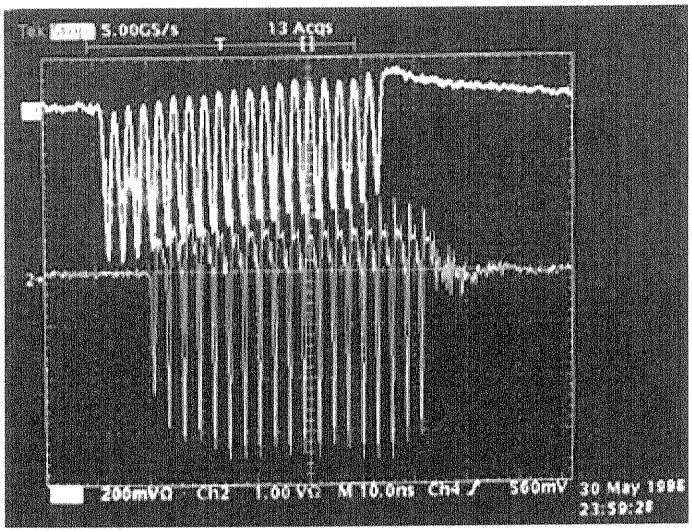

Figure C.16: Extracted Multi-bunch beam. Upper is emission current monitored by CT just down stream of the gun and lower waveform is measured by WC at down stream of first accelerating structure.

References

[1] C. Wyss. The LEP Energy Upgrade Project. *1991 IEEE Part. Accel. Conf.*, page 150, 1991.

[2] H. Henke. Study work on the CERN Linear Collider (CLIC). *CERN-LEP-RF*, **89-62**, 1989.

[3] K. Balewski et al. Status report of a 500 GeV S-band linear collider study . *DESY*, **91-153**, 1991.

[4] N. Holtkamp. The s-band linear collider test facility. *DESY M*, **96-13**, Jul 1996.

[5] R. Brinkmann. The TESLA superconducting linear collider. *DESY-M*, **97-04**, 1997.

[6] The NLC Design Group. Zeroth-Order Design Report for the Next Linear Collider. *LBNL-PUB-5424, also SLAC Report 474 or UCRL-ID-124161*, May 1996.

[7] E.A. Kushnirenko. VLEPP: STATUS REPORT. *Proceedings, e+ e- collision physics*, pages p538–551, 1989.

[8] JLC Design Study Group. JLC Design Study. *KEK-Report*, **97-1** , 1997.

[9] D. Burke. The Final Focus Test Beam project. *SLAC-PUB*, **5517**, 1991.

[10] D. Burke. Results from the final focus test beam. *SLAC-PUB*, **6609**, 1994.

[11] T. Shintake. Proposal of a nanometer beam size monitor for e+e- linear colliders. *Nucl. Instr. and Meth.*, **A311**:p453, 1992.

[12] T. Shintake et al. Experiments of nanometer beam size monitor at fftb using interferometry. *IEEE PAC Dallas*, 1995.

[13] P. Puzo et al. FIRST RESULTS OF THE ORSAY BEAM SIZE MONITOR FOR THE FINAL FOCUS TEST BEAM. *EPAC 94, LAL-RT*, **94-08**, 1994. Submitted to Nucl. Instrum. Methods.

[14] P. Puzo. Results of a gas-ionization beam size monitor at the Final Focus Test Beam. *LAL Preprint*, **98-28**, 1998. Submitted to Nucl. Instrum. Methods.

[15] K. Yokoya. Linear colider gaisetu. *OHO '95 High energy accelarator seminor*, 1995. in Japanese.

[16] P. B. Wilson. Linear accelerators for tev colliders. *SLAC-PUB*, **3674** , 1985.

[17] S. Takeda. Injector linac for linear collider. *OHO '95 High energy accelarator seminor*, 1995. in Japanese.

[18] M. Sands. The physics of electron storage rings. *SLAC*, **121** :172, 1970.

[19] K. Oide. Synchrotron-radiation limit on the forcusing of electron beams. *Phy. Rev. Letter*, **61**:1713, 1988.

[20] General Editor R. B. Neal. *THE STANFORD TWO-MILE ACCELERATOR*. W. A. Benjamin, Inc. New York Amsterdam, 1968.

[21] K. Yokoya. Linac etc. *Special lecuture in Nagoya University*, 1993. in Japanese.

[22] Y. Ogawa et al. Wakefield characteristic of higth-intensity, multibunch beam. *Nucl. Instr. and Meth.*, **A320**:405–412, 1992.

[23] Y. Ogawa et al. Longitudinal wake field characteristics of the kek positron generator linac. *KEK Preprint*, **91-29 A**, 1991.

[24] K. Kubo. Emittance preservation. *OHO '95 High energy accelarator seminor*, 1995. in Japanese.

[25] Jie GAO. Multibunch emittance growth and its correction in s-band linear collider. *Presented at the 17th Int. Linac Conf., Tsukuba,*, 1994.

[26] A. Mosnier. Instabilities in linacs. *Lecture given at the CERN Advanced Accelerator Physics cource*, 1993.

[27] T. Higo et al. Detuned accelerating structure for linear collider. *KEK Preprint*, **98-12**, 1998.

[28] R. H. Miller et al. A damped detuned structure for the next linear collider. *SLAC-PUB*, **7288** , 1997.

[29] T. Shintake. HOM free linear accelerator structure using choke mode cavity. *KEK Preprint*, **92-66**, 1992.

[30] K. Kubo. A simulation program for phase space dynamics in future linear colliders. *NLC Note*, 1995.

[31] Z. D. Farkas. Binary peak power multiplier and its application to linear accelerator design. *IEEE Trans. MTT-34*, page p1036, 1986.

[32] P. B. Wilson et al. SLED II :A New Method of RF Pulse Compression. *presented at the Linear Accelerator Conference, Albuquerque, New Mexico,SLAC-PUB*, **5330** , 1990.

[33] H. Mizuno and Y. Otake. A New RF Power Distribution System for X band Linac Equivalent to ann RF Pulse Compression Scheme of Factor 2^n. *KEK Preprint 94-112*, 1994.

[34] T. Shintake et al. A New RF Pulse-Compressor Using Multi Cell Coupled-Cavity System. *EPAC96, KEK Preprint*, **96-71**, 1996.

[35] T. Shintake et al. Development of C-band RF Pulse Compression System for e+e- Linear Collider. *PAC97, KEK Preprint*, **97-48**, 1997.

[36] F.-J. Decker et al. Reducting energy spread for long bunch train at slac. *SLAC-PUB*, **7214** , June 1996.

[37] N. Holtkamp et al. Transient beam loading compensation in travering wave linear accelerator. *DESY 96-043*, March 1996.

[38] P. B. Wilson. SLED: A Method for Doubling SLAC's Energy. *SLAC-TN*, **73-15** , 1973.

[39] A. Novokhatsky V. Balakin and V. Smirnov. VLEPP: Transverse Beam Dynamic. *Proc. of 12th Int. Conf. on High Energy Accelerators, Fermila*, 1983.

[40] J. T. Seeman et al. Measured Optimum BNS Damping Configuration of the SLC Linac. *SLAC-PUB*, **6204** , 1993.

[41] H. Matsumoto et al. High power test of a SLED system with dual sidewall coupling irises for linear collider. *Nucl. Instr. and Meth.*, **A330**, 1993.

[42] J. Urakawa et al. Gun trigger system for ATF. *Nucl. Instr. and Meth.*, **A352**:p207–209, 1994.

[43] T. Korhonen et al. R&d of the timing system. *Proc. of the 17th Int. Linac Conf., Tsukuba,*, page p831, 1994.

[44] H. Hayano. Submicron Beam Position Monitors for Japan Linear Collider. *Proc. of 16th Inte. Linac Conference*, 1992.

[45] H. Hayano. *FFIR Workshop, Atami, Shizuoka,Japan*, 1994.

[46] T. Naito. OTR monitor for ATF Linac. *Proc. of the 18th Int. Linac Conf., Geneva*, 1996.

[47] K. Oide et al. http://www-acc-theory.kek.jp/SAD/sad.html.

[48] M. Yoshida ET AL. Efficiency and gain enhancement of rf-pulse compressor for c-band rf system. *Proc. of the 19th Int. Linac Conf. LINAC98, Chicago*, 1998.

[49] C. Adolphsen et al. BEAM LOADING COMPENSATION IN THE NLCTA. *PAC97, SLAC-PUB*, **7518** , 1997.

[50] K. Yokoya et al. Short-range wake formulars for infinite periodic pillbox. *Private report*, May 1998.

[51] M. Yamamoto et al. Study of long-range wake-field in accelerating structure of linac. *KEK Report*, **94-9**, 1998.

[52] Y. Otake. Development of RF Phase Detector for JLC. *Proc. of the Second SLAC/KEK Linear Collider Workshop, Tsukuba, Japan*, 1988.

[53] H. Matsumoto and Y. Otake. Phasing System for 1 GeV Test Linac. *Proc. of the Second SLAC/KEK Linear Collider Workshop, Tsukuba, Japan*, 1994.

[54] H. Hinode et al. Atf accelerator test facility design and study report. *KEK-Internal*, **95-4**, 1995.

[55] H. Matsumoto et al. High Power Test of a High Gradient S-band Accelerator Unit for the Accelerator Test Facility. *Proc. of the 17th Int. Linac Conference, Tsukuba, Japan*, 1988.

[56] H. Hayano. ATF LINAC COMMISSIONING. *KEK Preprint*, **96-112** , 1996.

[57] S. Kashiwagi et al. PRELIMINARY TEST OF $\pm\Delta F$ ENERGY COMPENSATION SYSTEM. *KEK Preprint*, **96-110** , 1996.

[58] H. Hayano. Commissioning of atf damping ring. *KEK Preprint*, **97-158** , 1997.

[59] T. Naito et al. Single bunched beam generation using conventional electron gun for jlc injector. *PAC91*, 1991.

[60] T. Naito et al. Generation of multi-bunch beam with thermionic gun for japan linear collider. *LINAC92*, 1991.

[61] T. Naito et al. Multi-bunch beam with thermionic gun for atf. *KEK Preprint*, **94-103** , 1994.

[62] H. Hayano et al. Wire alignment syatem for atf linac. *Proc. of the 19th Linear Accelerator meeting in Japan*, page p287, 1994.

[63] S. Kashiwagi and H. Hayano. Calibration of stripline bpm for atf linac. *Proc. of the 20th Linear Accelerator meeting in Japan*, 1995.

[64] T. Asaka et al. Multi-bunch beam caracteristicsn for 80mev atf preinjector. *Proc. of the 20th Linear Accelerator meeting in Japan*, 1995.

[65] J. Urakawa. Kek/atf damping ring. *PAC97*, 1997.

[66] K. Kubo et al. TEST OF OPTICS DIAGNOSTICS IN ATF. *PAC97*, 1997.